AMORPHOUS ALUMINA OXIDATION PROTECTIVE COATINGS FOR ZIRCALOY BASED ON A COMPOSITIONAL GRADIENT LAYER SYSTEM

By

SANG TAE PARK

A DISSERTATION PRESENTED TO THE GRADUATE SCHOOL
OF THE UNIVERSITY OF FLORIDA IN PARTIAL FULFILLMENT
OF THE REQUIREMENTS FOR THE DEGREE OF
DOCTOR OF PHILOSOPHY

UNIVERSITY OF FLORIDA

2004

Copyright 2004

by

Sang Tae Park

Dedicated to my wife, Misun, whose love, trust, patience, encouragement and supports allowed me to be here.

ACKNOWLEDGMENTS

I can say that I am a happy man because I could meet many good people in Gainesville. First of all, I gratefully acknowledge Dr. Baney. He has not been my advisor. He has been my mentor, my senior in life, my supervisor, my schoolmaster, my consultant, my helper, my friend and even my father in Gainesville. He gave me not only the opportunity to do good research but also the comfortable atmosphere. He taught me not only the research but also the way to live my life among people. I'll never be able to forget all he has given me. I am grateful to Dr. Dow Whitney who has supervised my written work most carefully and always welcome me in his office whenever I knocked at his office, Dr. Paul Holloway who delivered his deep understanding about surface science in his lecture and authorized me to use the equipment for my research and showed me the way of managing a lab, Dr. Darryl Butt who gave me helpful advice with great smile and also let me use the equipment for hydrothermal study, and Prof. James Tulenko who I have worked with for a long while since my research started and gave me an opportunity and indispensable advice about the nuclear research field with which I was not familiar.

I cannot help giving thanks to Rob Owings with whom I could rebuild the 'Rusty' sputter, Jairaj in Dr. Butt's group about his assistant with autoclave, and to MAIC staff, especially, Eric Lambers for AES, Jerry Bourne for FIB and nanoindentation, Kerry Sieben for TEM, and Valentine Craciun for GAXRD.

I should appreciate the friendship and help of Jinho Kim, Noriko Shibuya, Paul Demkowicz, Lisa Argo, Dongwon Lee, Kyle Kathan, and Yunmi Kim in Dr. Baney's

group; and all my friends in Gainesville; and members in Eden pasture family, pastor Sohn and fellows in my church, who have been my comforter in Gainesville.

Above all, I would like to give all thanks to my God who is the reason and the way of my life. Finally, I sincerely acknowledge my family, especially my parents, whose love and encouragement helped me continue pursuing my dream. My wife and my two daughters have provided me the “Home” when I had been tired so that I could cheer up myself and get back to where I was supposed to be with peaceful mind. They have been my “Home” so far and forever. Words cannot be enough at all to express my love to them.

TABLE OF CONTENTS

Page

ACKNOWLEDGMENTS iv

LIST OF TABLES ix

LIST OF FIGURES x

ABSTRACT xiv

CHAPTER

1 INTRODUCTION 1

2 LITERTATURE REVIEW 4

- 2.1. Corrosion of Zircaloy Clad LWR Fuel Rods 4
    - 2.1.1. Zircaloy for nuclear applications 4
    - 2.1.2. Oxidation of Zircaloy in high-temperature water 8
    - 2.1.3. Oxidation stage of Zircaloy failure in pressurized water reactor 11
- 2.2. Sub-Critical Conditions 12
- 2.3. Recent Trends and Issues in Oxidation Protective Systems for Zircaloy 15
    - 2.3.1. Methods for current oxidation protective systems for Zircaloy cladding 15
        - 2.3.1.1. Metallurgical alloying 16
        - 2.3.1.2. Surface modification 17
        - 2.3.1.4. Overlay coating by vapor deposition 20
    - 2.3.2. Metal/ceramic interfaces 24
- 2.4. Requirements for Oxidation Protective Coating System 25
    - 2.4.1. Coating requirements 25
    - 2.4.2. Material selection 26
- 2.5. Aluminum Oxide Coatings 27
    - 2.5.1. Properties of alumina coatings 28
    - 2.5.2. Alumina in sub-critical aqueous conditions 29
    - 2.5.3. Phase transformation and temperature dependence of alumina 30
- 2.6. Compositional Gradient Coatings 31
    - 2.6.1. Concept 31
    - 2.6.2. Processes and applications 33
    - 2.6.3. Issues on FGM 34

3 EXPERIMENTAL 36

3.1. Introduction 36
3.2. Substrate material 36
3.3. Coating processes 37
    3.3.1. Alumina ceramic coating by RF magnetron sputtering system 37
    3.3.2. Aluminum metal deposition by electron beam evaporation 38
3.3. Heat treatments 40
3.4. Coating Characterizations 40

4 PROPERTIES OF AMORPHOUS ALUMINA THIN FILMS 50

4.1. Introduction 50
4.2. Annealing Temperature Dependence and Thermal Stability 50
    4.2.1. Microstructure Of Sputter Deposited Alumina Films On Zircaloy 52
    4.2.2. Mechanical Properties 57
    4.2.3. Influence of Sputtering Gas Ratio on Stochiometry 62

5 CONTINUOUS COMPOSITIONAL GRADIENT COATINGS THROUGH CONTROLLED HEAT TREATMENT OF ALUMINUM FILMS ON ZIRCALOY64

5.1. Introduction 64
5.2. As-Deposited Aluminum Metal Coatings 66
5.3. Temperature Dependence 67
5.4. Annealing Time Dependence 69
5.5. Thickness Dependence 71
5.6. Controlled Two-Step Heat Treatment 74
5.7. Phase Identification 75
5.8. Cross-sectional TEM and in-situ EDS 78
5.9. Atomistic and Thermodynamic Considerations 82
5.10. Summary 85

6 EFFECT OF COMPOSITIONAL GRADIENT LAYER AS AN INTERLAYER BETWEEN AMORPHOUS ALUMINA THIN FILM AND ZIRCALOY SUBSTRATE 86

6.1. Introduction 86
6.2. Proposed Model for Oxidation Protection System 87
6.3. Prevention of the Formation of Zirconium Oxide 87
6.4. Improvement of Adhesion 89

7 BEHAVIOR OF SPUTTER-DEPOSITED AMORPHOUS ALUMINA THIN FILMS IN SUBCRITICAL HYDROTHERMAL CONDITIONS 95

7.1. Introduction 95
7.2. The behavior of amorphous alumina thin films in subcritical water 96
7.3. Summary 102

8 CONCLUSIONS..104

LIST OF REFERENCES..106

BIOGRAPHICAL SKETCH..146

LIST OF TABLES

Table page

2.1. Thermal neutron capture cross section of various materials 31

2.2. Typical physical and mechanical properties of zirconium 32

2.3. Structures and annealing behaviors of Al2O3 films synthesized by various PVD methods. [13, 58, 59] 57

3.1. Chemical composition of Zircaloy-4. 64

3.2. Test conditions for scratch analysis of samples 76

5.2. Thermodynamic data for alumina top layer [110] 112

6.1. Critical forces for the delaminations of the amorphous alumina films (a) without and (b) with the compositional gradient interlayer 123

LIST OF FIGURES

Figure page

2.1. Zircaloy/zirconium oxide/water interface 35

2.3. Course of ionic product, density, and dielectric constant of water versus temperature at a pressure of 24 MPa [36] 40

2.4. Interdependences of the corrosion-determining factors in high-temperature aqueous solutions. [36] 41

2.5. Homophase boundaries and heterophase boundaries 52

3.1. (a) Schematic diagram of cross-sectional view and (b) picture of the sputter deposition system 66

3.2. Schematic of the electron beam evaporation system 67

3.3. The diagram of the fundamental components of the Nano-Scratch Tester 75

3.4. The picture of autoclave system used for hydrothermal testing 76

4.1. XRD spectrum of (a) Zircaloy substrate only, (b) as-deposited, (c) 550°C annealed (d) 650°C annealed and (e) 800°C annealed Al_2O_3 coatings on Zircaloy substrates, using RF magnetron sputtering. Annealing was performed in air for 2 hours. 80

4.2. XRD spectra of the amorphous alumina coated Zircaloy annealed at 500°C for 2h (a) and that of the uncoated Zircaloy substrate annealed at 500°C for 2h (b) 82

4.3. AES depth profiles of (a) as-deposited, (b) 450°C annealed, (c) 500°C annealed and (d) 550°C annealed Al_2O_3 coatings (on next page) on Zircaloy substrates, using RF magnetron sputtering. Annealing was performed in air for 2 hours 83

4.3. AES depth profiles of (a) as-deposited, (b) 450°C annealed, (c) 500°C annealed and (d) 550°C annealed Al_2O_3 coatings on Zircaloy substrates, using RF magnetron sputtering. Annealing was performed in air for 2 hours (continued from previous page) 84

4.4. AFM images of (a) as-deposited, (b) 500°C annealed and (c) 800°C annealed Al_2O_3 coatings on Si substrates, using RF magnetron sputtering. Annealing was performed in air for 2 hours 85

4.5. Surface scan profiles of the Zircaloy substrates polished with different grit size or suspension particle size used as polishing media; polished with (a) 600grit SiC paper, (b) 5μm alumina particles and (c) 1μm alumina particles............................ 86

4.6. Nano indentation load-unload curves of the sputter deposited amorphous thin films; (a) as-deposited, (b) annealed at 500°C and (c) annealed at 800°C for 2 hours in air87

4.7. Hardness and modulus plots and graphs of the sputter deposited amorphous thin films; (a) as-deposited, (b) annealed at 500°C and (c) annealed at 800°C for 2 hours in air.. 89

4.8. The variation of (a) aluminum and (b) oxygen concentration in the deposited films with varying ratio of oxygen reactive gas to argon sputtering gas during the sputter deposition 91

5.1. AES depth profile of an aluminum metal film with the thickness of 500nm deposited on a Zircaloy substrate by electron beam evaporation. 95

5.2. EDX analysis results of an aluminum metal film deposited onto a Zircaloy substrate by electron beam evaporation.. 95

5.3. The AES depth profiles of the oxidized aluminum films on Zircaloy with a thickness of 300 nm after annealing for 2 hours at various temperature of (a) 400°C, (b) 500°C and (c) 600°C, respectively. 96

5.4. The AES depth profiles of the oxidized aluminum films on Zircaloy with a thicknesses of 100 nm after annealing at 500°C for various times of (a) 1 hour, (b) 2 hours and (c) 3 hours, respectively... 98

5.5. The AES depth profiles of the oxidized aluminum films on Zircaloy with a thicknesses of 300 nm after annealing at 500°C for 3 hours.................................. 99

5.6. The SEM pictures of the oxidized aluminum films whose thickness of (a) 100 nm, (b) 300 nm and (c) 5000 nm on Zircaloy after annealing at 500°C for 2 hours.... 100

5.7. AES depth profiles of a 300 nm aluminum films oxidized at 650°C for 30min followed by at 500°C for 2hrs: peak height and atomic concentration are marked on y-axis in (a) and (b), respectively 102

5.8. SEM micrograph of a 300 nm aluminum film deposited on Zircaloy after (a) oxidizing at 500°C for 3hrs and (b) oxidizing at 650°C for 30min followed by at 500°C for 2hrs 103

5.9. GAXRD (glancing angle incident x-ray diffraction) spectra of a 300 nm aluminum film deposited on Zircaloy annealed (a) at 650°C for 30min followed by at 500°C for 2hrs, (b) at 650°C for 30min and (c) as-deposited (no annealing) 104

5.10. AES multiplex spectra in correspondence with depth profiles for (a) Al and (b) O of the 300 nm aluminum films oxidized at 650°C for 30 minutes followed by at 500°C for 2 hours. (in Fig.5.7) 106

5.11. Cross-sectional TEM pictures of the 300 nm aluminum films oxidized at 650C for 30 minutes followed by at 500C for 2 hours 108

5.12. EDS line scan spectra of the $Al_2O_3/Al_3Zr/Al_2Zr_3$/Zircaloy structure shown in the TEM image (Fig.5.11) 110

5.13. The plots with the thickness of EDS results of the 300 nm aluminum films oxidized at 650C for 30 minutes followed by at 500C for 2 hours 111

6.1. The schematics of (a) the model based on Al-Zr phase diagram in equilibrium and (b) the model completed by the experimental using the controlled heat treatment.117

6.2. XRD spectra of (a) the aluminum film oxidized at 650C for 30 minutes followed by at 500C for 2 hours (Fig.5.9. (b)) and (b) that of the uncoated Zircaloy substrate step-annealed 118

6.3. TEM images of amorphous alumina thin film on the aluminum film oxidized at 650C for 30 minutes followed by at 500C for 2 hours 119

6.4. The optical microscope images after scratch tests for (a) amorphous alumina film on Zircaloy and (b) amorphous alumina film Zircaloy with the compositional gradient interlayer 122

6.5. The Comparison graph of the critical forces for the delaminations of the amorphous alumina films with and without the compositional gradient interlayer 124

7.1. SEM image (a) and AES depth profile (b) of as-deposited alumina coatings on Zircaloy 126

7.2. Hydrothermally grown crystallites after autoclave exposure to subcritical aqueous condition: outer layer (a), inner layer (b) and EDX line scan profile (c). 127

7.3. EDX spectrum and line-scan profile of bottom layer through top layer of sputter-deposited alumina film after autoclave test. 128

7.4. XRD spectra of sputter-deposited alumina coating after autoclave test compared with as-deposited alumina film and Zircaloy substrate. Boehmite peaks appeared after autoclave exposure. 129

7.5. XPS survey spectra and multiplex peaks of sputter-deposited alumina coating before (a and b) and after (c and d) autoclave exposure, respectively. 130

7.6. Morphology change of AlOOH particles with variation of chemical species distribution [125]

7.7. Variation of AlOOH solubility with temperature [119] 132

7.8. TEM image of hydrothermally grown crystallite of AlOOH in subcritical condition after autoclave test 133

Abstract of Dissertation Presented to the Graduate School
of the University of Florida in Partial Fulfillment of the
Requirements for the Degree of Doctor of Philosophy

AMORPHOUS ALUMINA OXIDATION PROTECTIVE COATINGS FOR ZIRCALOY BASED ON A COMPOSITIONAL GRADIENT LAYER SYSTEM

By

Sang Tae Park

August 2004

Chair: Ronald H. Baney
Major Department: Materials Science and Engineering

Light water reactor (LWR) fuel performance is currently limited by thermal, chemical, and mechanical constraints associated with the design, fabrication, and operation of fuel in a nuclear environment. These limits constrain the lifetime of the fuel, the maximum power at which fuel can be operated, the probability of fuel failure over the core lifetime, and the transient and safety performance of the fuel during postulated accidents. Waterside corrosion of the Zircaloy cladding encasing the uranium oxide pellets is one of the primary factors limiting high “burn up” of nuclear fuel in pressurized water reactor (PWR) nuclear reactors. High “burn up” can significantly impact plant safety and economics.

Amorphous aluminum oxide coatings with aluminum-based compositional gradient layers (CGLs) were fabricated to develop ceramic coating corrosion protection systems for Zircaloy fuel rod cladding in pressurized water reactor (PWR) nuclear reactors. Aluminum films were deposited on Zircaloy substrates by electron-beam evaporation, and surface-alloyed by controlled heat treatment at near the melting temperature of aluminum. Two step heat treatment procedures were used to make compositional gradient compound layers. Aluminum film thickness, air annealing time and temperature were

varied. Morphology, elemental composition and compositional depth profile for the deposited films were characterized using field emission scanning electron microscopy (FE SEM), energy dispersive x-ray analysis (EDX), and auger electron spectroscopy (AES), respectively. The AES analysis of the oxidized coatings showed that gradient compositions were obtained as expected (with Al, Zr, and O content varying through the coating thickness). Glancing angle x-ray diffraction (GAXRD) analysis also showed that a variety of intermetallic and oxide phases (such as Al_3Zr, Al_2Zr_3, Al_2O_3, ZrO_2 and Zr_3O) were formed in the coatings during processing. The intermetallic layers improved the adhesion property of the alumina top overcoating to Zircaloy metal substrate, and functioned as oxidation resistant layers.

We successfully constructed the compositional gradient layer structure for the improvement of adhesion and thermal stability and for the integrated interfaces. It was previously reported that pure bulk alumina and amorphous ceramic coatings were stable in hydrothermal water conditions and acidic solutions, respectively. However, the amorphous alumina coatings in our study were not stable under nuclear reactor conditions of subcritical water at 350°C and 20.1 MPa (3000 psi).

Subcritical aqueous solutions have recently received much attention because of their promising properties such as a lower dielectric constant and high dissolvability. They are an integral part of pressurized water reactor (PWR) systems. Therefore, many materials and surface modifications have been studied for reactor protection in subcritical conditions. We investigated the behavior of amorphous alumina thin films deposited on Zircaloy substrates by rf magnetron sputtering, in the near-supercritical hydrothermal water conditions. When uniformly deposited alumina coatings were exposed to

subcritical hydrothermal conditions, hydrothermal crystallite formation was observed. Surface morphology was characterized by FE SEM and compositional analyses were performed using AES, EDX analysis, and EDX line scan. Hydrothermally grown well-faceted particulates after exposure to autoclave were observed and identified to be aluminum hydroxide, boehmite (γ-AlOOH) by XRD spectra, peak shift in x-ray photoelectron spectroscopy (XPS) and transmission electron microscopy (TEM) images. We hypothesized the mechanism of the boehmite formation as the dissolution of amorphous alumina and the reprecipitation of boehmite during the cooling process.

CHAPTER 1
INTRODUCTION

Light water reactor (LWR) fuel performance is currently limited by thermal, chemical, and mechanical constraints associated with the design, fabrication, and operation of fuel in a nuclear environment [1, 2]. These limits constrain the lifetime of the fuel, the maximum power at which fuel can be operated, the probability of fuel failure over the core lifetime, and the transient and safety performance of the fuel during postulated accidents. Waterside corrosion of the Zircaloy cladding encasing the uranium oxide pellets is one of the primary factors limiting high "burn up" of nuclear fuel in pressurized water reactor (PWR) nuclear reactors. High "burn up" can significantly impact plant safety and economics.

Most attempts to prevent corrosion of Zircaloy have been made by optimizing the metallurgical composition and processing of the Zircaloys [3]. Recently, surface treatments using high-energy beam such as ion implantation have been studied to improve the corrosion properties of the cladding surfaces [4-6].

Ceramic surface coatings have been used in various fields as protective coatings such as thermal barrier coatings [7-12], wear protective coatings [13-15], and corrosion protective coatings [16-22]. Only a few studies have been reported for PWR cladding protection. Thin surface coatings have been suggested as a possible means for Zircaloy cladding corrosion prevention [22-26]. Ceramic coatings are increasingly being used to protect metals in corrosive environments, because of their suitable properties, and the possibility of connecting them to metals. However, the coating may easily fail because of the poor bonding between the ceramic coating and the metal substrate. Their limitations are not generally due to the ceramic coating itself but rather the interface quality (such as adhesion) that is reflected by the fracture resistance of the metal/ceramic interface [27-29].

It has been reported that functionally gradient coatings have been used to improve the adhesion properties by reducing the thermal expansion mismatch and the interfacial stresses between the coating and substrate. This thermal expansion mismatch and the stresses are responsible for interface delamination and film spalling damage [30, 31]. Functionally gradient materials (FGMs) can be considered as a sort of composite, whose composition varies with thickness according to performance requirements. Such materials have the potential for a wide range of thermal and structural applications, including thermal gradient structures, wear and corrosion resistant coatings, and metal/ceramic joining. The coating is fabricated to be a composite, with the local volume fraction of metal varying through the coating thickness, mimicking an inclusion/matrix type FGM or a FGM multilayer.

Alumina (Al_2O_3) is very well known for its chemical stability, mechanical strength, and low cost. For these reasons, alumina coatings have been used for protective layers such as diffusion barriers [32], thermal barrier coatings [10], and wear resistant [33] and corrosion resistant coatings [34]. Our study aimed to develop a ceramic-coating corrosion-protection system for Zircaloy cladding used in pressurized water reactors (PWRs). Alumina was selected as the most probable candidate, because of its appropriate properties such as thermal expansion coefficient, thermal conductivity, thermal flux, and neutron cross-section according to our previous research [35].

We proposed the compositional gradient layer through controlled heat treatment with amorphous alumina overcoating as a corrosion protection system for the Zircaloy cladding in PWR. Aluminum films were deposited on Zircaloy substrates by electron-beam evaporation, and were heat-treated by controlled annealing at near the melting temperature of aluminum. Two different annealing procedures were used to make compositional gradient compound layers. Aluminum film thickness, and air oxidation time and temperature were varied to optimize the film structure. In a second step, amorphous alumina overcoatings were deposited on the compositional gradient layers, by RF magnetron sputtering. Their structural, compositional and mechanical properties were characterized. In addition, the behaviors of the sputter-deposited amorphous alumina thin films under subcritical hydrothermal water conditions were investigated, and their mechanism of the phase change was discussed.

CHAPTER 2
LITERATURE REVIEW

2.1 Corrosion of Zircaloy Clad Light Water Reactor (LWR) Fuel Rods

Almost all power reactors in the world are cooled by either normal or heavy water, and are termed light water reactors (LWRs) or heavy water reactors (HWRs), respectively. The heat-generating fuel elements, or fuel rods, are made of stacks of uranium dioxide (UO_2) pellets clad or sheathed in hermetically sealed tubes. Fuel rods are grouped together in assemblies whose designs differ markedly according to the type of reactor. [36]

A primary consideration for fuel-assembly reliability is the ability to maintain optimum power generation over the design lifetime of the assembly, without releasing the radioactive by-products of the nuclear fission process into the primary coolant (water). Therefore, the cladding tubes separating the coolant water from the nuclear fuel and its by-products must resist the corrosive attacks of both environments, while meeting all mechanical loads present or anticipated during power and fuel-handling operations.

2.1.1 Zircaloy for Nuclear Applications

Although the first LWRs in the United States used stainless steel as a cladding material, the economics of LWR-generated electricity favor the use of zirconium-base alloy (Zircaloys), wherever possible, in the high-flux regions of the reactor core. The reason for this is the low neutron-absorption cross-section of zirconium. As a result, most tubes and other assembly structural components are made of zirconium alloys.

Materials for fuel cladding and structural components in nuclear reactors are restricted because of the following crucial requirements:

- Low absorption cross-section for thermal neutrons
- Adequate strength, creep resistance, and ductility after prolonged irradiation in the reactor coolant
- Excellent corrosion and oxidation resistance
- Absence of interactions with the fuel material and fission products

Zirconium alloys, such as the Zircaloys and Zr-2.5Nb, have been developed to meet these requirements. In water-cooled reactors, zirconium alloys have found extensive use for fuel cladding and as pressure tubes. In systems in which the first requirement listed above is of overriding importance for reasons of neutron physics (Table 2.1), the choice is virtually restricted to zirconium or one of its alloys.

Table 2.1. Thermal neutron capture cross-section of various materials

Element or alloy	Thermal neutron cross section (barns)
Magnesium	0.059
Zirconium	0.18
Zircaloy-4	0.22
Aluminum	0.22
Tin	0.65
Iron	2.4
300 series stainless steel	3.1
Titanium	5.6
Hafnium	113
Cadmium	2.4×10^3

Typical physical and mechanical properties of zirconium are given in Table 2.2 for comparison with the properties of other structural metals. First, the density of zirconium is lower than that of iron or nickel. Second, zirconium has a low coefficient of thermal expansion. The coefficient of thermal expansion of zirconium is about two-thirds that of titanium, about one-third that of AISI type 316 stainless steel, and about one-half that of Monel. Third, zirconium has high thermal conductivity that is about 18% better than type 316 stainless steel.

Table 2.2. Typical physical and mechanical properties of zirconium

Physical Properties		
Atomic radius, Å	0 charge	1.60-1.62
	4+ charge	0.80-0.90
Density, g/cm^3 (lb/in.^{3})		6.510 (0.235)
Crystal structure	α phase	Hexagonal close-packed (below 865 °C, or 1590 °F)
	β phase	Body-centered cubic (above 865 °C or 1590 °F)
Melting point, °C (°F)		1852 (3365)
Coefficient of thermal expansion, per °C at 25 °C (75 °F)		5.89×10^{-6}
Thermal conductivity (300-800 K)		21.5 W/m·K (12.7 Btu·ft/h·ft^2·°F)
Latent heat of fusion, cal/g		60.4
Latent heat of vaporization, cal/g		1550
Mechanical Properties		
Modulus of elasticity, MPa (ksi)		9.9×10^4 (14.4×10^3)
Poisson's ratio (ambient temperature)		0.35

The primary zirconium alloys are known as Zircaloy-2 and Zircaloy-4. They are mostly zirconium (98 wt%) with low amounts of alloying elements (tin, iron, chromium, nickel, and oxygen), which confer to the alloys the desirable mechanical and corrosion properties. The corrosion resistance of Zircaloys depends on a number of factors that include the concentration and distribution of alloying elements and impurity elements.

Zircaloy-2 is superior to unalloyed zirconium in high-temperature water and steam. A tightly adherent oxide film forms on this alloy at a rate that is at first quasi-cubic, but after an initial period undergoes a transition to linear behavior. Unlike the oxide film on unalloyed zirconium, the oxide film on Zircaloy-2 remains dark and adherent throughout transition, and in the post-transition region.

Zircaloy-4 differs in composition from Zircaloy-2 only in having no nickel, and a slightly greater iron content. Both variations are intended to reduce hydrogen pickup in reactor operation. The corrosion behavior of Zircaloy-4 is very similar to that of Zircaloy-2. However, hydrogen pickup for Zircaloy-4 is significantly lower, particularly when the alloy is exposed to water at 360°F. At this temperature, hydrogen pickup for Zircaloy-4 is about 25% of theoretical, or less than half that for Zircaloy-2.

Zirconium and most of its alloys exhibit strong anisotropy, because of two characteristics of the metal: Zirconium has a hexagonal close-packed (hcp) crystal structure at room temperature, and it undergoes allotropic transformation to a body-centered cubic (bcc) structure at about 870°C (1600°F). The strong anisotropy profoundly influences the engineering properties of zirconium and its alloys, and must be taken into account when selecting and processing a zirconium metal. Zirconium forms intermetallic compounds with most metallic elements, and only a limited number of alloys have been developed. For nuclear service, it is desirable to have zirconium alloys with improved strength and corrosion resistance in high-temperature water or steam. The most common zirconium alloys (Zircaloy-2 and Zircaloy-4) contain the strong α stabilizers tin and oxygen, as well as the β stabilizers iron, chromium, and nickel. There is an extensive $\alpha + \beta$ field from about 790 to 1010°C (1450 to 1850°F). Iron, chromium, and nickel form intermetallic compounds, and the distribution of these compound phases is critical to the corrosion resistance of the alloys in steam and hot water.

Zirconium is a reactive metal, as evidenced by its redox potential of -1.53 V versus the normal hydrogen electrode at 25°C (75°F). It has a high affinity for oxygen. When zirconium is exposed to an oxygen-containing environment, an adherent, protective oxide film forms on its surface.

The high corrosion resistance of zirconium alloys results from the natural formation of a dense stable oxide on the surface of the metal like unalloyed zirconium. This film is self healing, it continues to grow slowly at temperatures up to approximately 550 °C (1020 °F), and it remains tightly adherent.

2.1.2 Oxidation of Zircaloy in High-Temperature Water

Light water reactors normally operate with a coolant temperature between 250 and 350 °C (480 and 660 °F) at a pressure of approximately 15 MPa (2200 psi) (PWRs). Therefore, out-of-reactor corrosion studies are usually conducted in high-pressure autoclaves, in which the water is in the liquid state at temperatures up to approximately 360 °C (680 °F). Under these conditions, the attack of Zircaloy by water is generally uniform.

The reaction between Zircaloy and water can be written as

$$Zr + 2H_2O \rightarrow ZrO_2 + 2(1 - x)H_2 + 4 \times H \qquad (2\text{-}1)$$

where the first and second left-hand terms represent zirconium and water, respectively; the right-hand terms represent zirconium oxide, hydrogen that is released into the corroding water, and hydrogen that is picked up by the Zircaloy; x is the pickup fraction. The pickup of hydrogen by the Zircaloy substrate leads to changes in its mechanical properties and, in particular, to a loss of ductility.

The formation of zirconium oxide results in a loss of metallic Zircaloy. Because the Pilling-Bedworth ratio is equal to 1.56 at ambient temperature, a given loss in metal thickness results in a larger gain in oxide thickness the molar volume ratios between the substrate and the oxide layer. The Pilling–Bedworth ratio (PBR) is the ratio of the volumes of oxide produced to the metal consumed by oxidation.{} Ratios of 1.0 or greater result in complete surface coverage by oxide and, usually, protective behavior and have oxide densities high enough to give a protective or passivating oxide layer. In Figure 2.1, the positions of the Zircaloy/ZrO_2 and ZrO_2/H_2O interfaces are shown relative to the position of the original Zircaloy/H_2O interface.

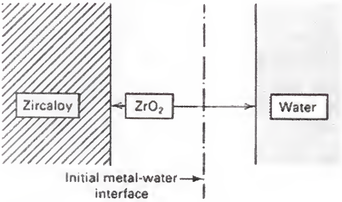

Figure 2.1. Zircaloy/zirconium oxide/water interface

The kinetics of the uniform corrosion reaction can be conveniently divided into two main periods, referred to as pre-transition and post-transition. In the first of the periods, a black coherent oxide film is formed, and the corrosion rate diminishes with time according to a rate law given by the simplified form:

(weight gain) = constant x $(\text{time})^n$

with the exponent n in the range of 0.25 to 0.5.

A transition follows to a period where the rate law is closer to linear ($n \cong 1$). This transition is eventually accompanied by a conversion of the black oxide to a gray or white oxide. The corrosion kinetics of Zircaloy in high-temperature water actually follow a periodic behavior, and the apparently linear dependence of the post-transition rate is obtained by averaging the time-dependent rates over several periods. A progressive acceleration of the post-transition rate, especially after sufficiently long reaction times, has also been shown.

Given that zirconium is a very reactive metal, it should readily corrode according to Eq. 2-1. However, because of the protective nature of at least part of the oxide film, Zircaloy belongs to the group of extremely corrosion-resistant alloys. The film acts as a barrier through which the reactive species (oxygen ions, electrons, etc.) must diffuse to sustain the corrosion reaction. During pre-transition, reaction rates are determined by diffusion through a surface film of increasing thickness. For the transition, which typically occurs when the oxide layer is 2 to 3 μm thick, part of the film undergoes a change in morphology and becomes non-protective. During post-transition, the thickness of the protective part of the oxide film successively increases and abruptly decreases. As discussed in the previous paragraph, linearization over a sufficiently long period of time can be readily performed. This is equivalent to assuming the existence of a protective barrier of constant thickness. Under typical high-temperature water autoclave conditions, this equivalent thickness is about 1 μm.

The out-of-reactor corrosion properties of Zircaloys are, in general, strongly dependent on the material microstructure and on temperature. In some cases, these properties also depend on the water chemistry conditions.

Zircaloy corrosion in PWRs has become an area of prime concern from a fuel performance point of view. In particular, fuel failures and plant derating due to corrosion have occurred in plants that combine high coolant temperature and high heat flux.

Therefore, the full economic benefits associated with high thermal efficiency, high burnup, higher-pH coolant (by adding greater amounts of LiOH), and higher fuel utilization (by fuel rod design changes) may not be obtainable in many existing plants without some improvement in the corrosion properties of the current zirconium alloys.

2.1.3 Oxidation Stage of Zircaloy Failure in Pressurized Water Reactor

Zircaloy-4 has a high affinity for oxygen and hydrogen with a preference for interaction with oxygen to form zirconium oxide (zirconia). An oxide film is formed on the waterside external surface by interaction of the clad with the dissolved oxygen in the water.

This dense oxide layer initially provides a protective coating toward further oxidation and a barrier to external hydriding. This is predicted by the molar volume ratios between the substrate and the oxide layer. Such a ratio is called the Pilling–Bedworth ratio (PBR). Zirconium is reported to have a PBR of 1.56.

Recent reports in the literature have delved more completely into the details of the mechanism of oxidation of Zircaloys. A thin, dense interfacial layer between the substrate metal and oxide gradually gives way to a less dense layer and transforms from tetragonal ZrO2 to monoclinic ZrO2. As the oxide layer grows compressive stresses are built up. The exact course of the corrosion is dependant on many factors. These include the chemical composition of the alloy, the temperature range of the oxidation investigation, surface topography, grain size and grain orientation, wet or dry environments, the pH and other water chemistry parameters in wet environments, as well as pressure. Radiation effects also complicate the course of the corrosion.

In general, the corrosion follows two steps. A dense tightly adhering oxide layer grows following a quasi-cubic rate law in the first step. As stresses begin to build in both the oxide layer and substrate metal due to the change in density of the oxide relative to the substrate metal (PBR = 1.54), cracks and pores begin to develop as a relief mechanism and the oxidation rate law switches to a linear form. It is undoubtedly the pores and cracks, which provide the failure pathways, which result in spallation. The oxidation rates are controlled by the transport of oxygen ions through the zirconium oxide. With the dense under layer of the oxide being broken by cracking and therefore providing shorter pathways for oxygen transport, corrosion is accelerated. It is needed to find a way to extend the time before the transition from a quasi-cubic rate process to linear rate process.

2.2 Subcritical Conditions

Water becomes supercritical fluid above 374°C and 22.1 MPa, and behaves entirely differently from water at ambient conditions. For example, at the critical point, the density, the viscosity and the dielectric constant decreases to 0.3 mg ml^{-1}, 0.05 cp, and 6, respectively. The increase in the temperature, while keeping the water in liquid state, leads to a dramatic decrease in its viscosity and dielectric constant even below the critical point. Sub-critical condition is called the region below the critical point but above the boiling temperature of water. Especially, the region near the critical point in the subcritical region has been of interests because of its unique properties such as high ionic product, relatively low density and dielectric constant.

During the last two decades, high-temperature (sub-critical) and supercritical water has been found to be a promising medium for different processes like chemical reactions, salt separation processes, extractions, ceramic processing, analytical applications and the oxidation of organic wastes (supercritical water oxidation; SCWO). In parallel with the increasing number of applications, the need for reactor materials that can withstand the

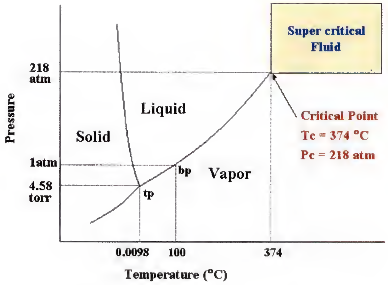

Figure 2.2. Phase diagram for water

harsh conditions has recently increased.

The physical properties of water have been investigated and reviewed in detail by Franck. [37-39] Kritzer reported the variations of the course of density, dielectric constant, and ionic product versus temperature at a constant pressure of 24MPa as shown in Figure 2.3. At a constant pressure, the values of density and of dielectric constant decrease with increasing temperature. Owing to the endothermic character of H_2O dissociation, the course of the ion product goes through a maximum at about 300°C. In the vicinity of the critical point (T_k=374°C; p_k = 22.1MPa), all parameters drop to low values at p_k. Generally, dissociation follows the course of solvent density and thus, decreases with increasing temperature and decreasing pressure.

In high-temperature water, where chemical reactions are accelerated, the transformation of a solid, thermodynamically unstable oxide towards a soluble, thermodynamically stable species should be fast. Thus, the importance of kinetic control decreases with temperature. This is in contrast to corrosion at ambient conditions, where

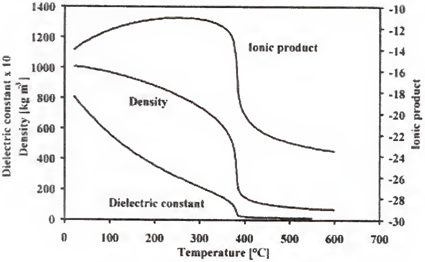

Figure 2.3. Course of ionic product, density, and dielectric constant of water versus temperature at a pressure of 24 MPa [40]

metals are often protected by a kinetically but not thermodynamically stable oxide layer.

At constant electrochemical potential, the pH region of highest stability depends on the oxide itself and might change with temperature. At constant pH value, electrochemical dissolution is observed for most metals. The dissolution is a common

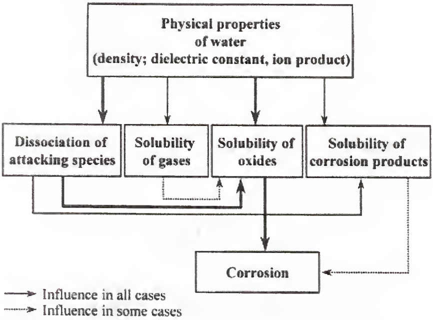

Figure 2.4. Interdependences of the corrosion-determining factors in high-temperature aqueous solutions [40]

phenomenon in high temperature solutions.

Corrosion of many materials depends on the physical properties of water in many ways. The corrosion-determining factors and their interdependences are illustrated in Figure2.4. Corrosion can slow down with an increase in temperature when the ionic product and density decrease simultaneously in supercritical region. However, corrosion also can be high in high-density aqueous solutions even at high temperatures [41-44], since electrochemical corrosion is an ionic phenomenon and its extent depends on the ionic character of the solvent.

2.3 Recent Trends and Issues in Oxidation Protective Systems for Zircaloy Cladding

2.3.1 Methods for Current Oxidation Protective Systems for Zircaloy

Many metals including zirconium that we discuss are inherently unstable in structures. Their ionic solutions and their carbonates, hydroxides, oxides, sulfides, sulfates, and many other salts are more stable than the free metal under the many conditions to which these metals are exposed. The free energy change for the conversion of these metals to a compound is a large negative value, and the thermodynamic driving force to convert the elemental metal to an oxide or salt is great. Thus, to retain a required physical properties of the metal, such as strength, thermal conductivity, magnetic nature, or electrical conductivity, it is essential to protect the metal from the environments to which it is expected to be exposed. These protection methods can be divided into the following: thermodynamic protection, kinetic protection, barrier protection, structural design, environmental control, and metallurgical design. This section will introduce some important methods which can be used for Zircaloy cladding protection among the various methods being used to protect a metallic system against corrosion. : metallurgical alloying, surface modification such as ion implantation and laser processing, and overlayer coating mainly using vapor deposition.

The objective of most protective systems is to reduce the rate of corrosion to a value that is tolerable or that will allow the material to attain its normal or desired lifetime. Only in a limited number of cases must corrosion protection be designed to eliminate corrosion completely.

2.3.1.1 Metallurgical Alloying

One of the primary reasons for producing alloyed metal is to improve corrosion resistance. The structure and composition of both metals and alloys are important in deciding their corrosion characteristics. Indeed, structure and composition are critical in many forms of localized corrosion.

Alloys for the nuclear industry have already been developed and being used widely. Materials for fuel cladding and structural components in nuclear reactors are restricted because of the following crucial requirements:

- Low absorption cross section for thermal neutrons
- Adequate strength, creep resistance, and ductility after prolonged irradiation in reactor coolant
- Excellent corrosion and oxidation resistance
- Absence of interactions with the fuel material and fission products

Zirconium alloys have been developed to meet these requirements. The primary zirconium alloys are known as Zircaloy-2 and Zircaloy-4. They are mostly zirconium (98 wt%) with low amounts of alloying elements (tin, iron, chromium, nickel, and oxygen), which confer to the alloys the desirable mechanical and corrosion properties. The corrosion resistance of Zircaloys depends on a number of factors that include the concentration and distribution of alloying elements and impurity elements.

Zircaloy-2 is superior to unalloyed zirconium in high-temperature water and steam. A tightly adherent oxide film forms on this alloy at a rate that is at first quasi-cubic but after an initial period undergoes a transition to linear behavior. Unlike the oxide film on unalloyed zirconium, the oxide film on Zircaloy-2 remains dark and adherent throughout transition and in the post-transition region.

Zircaloy-4 differs in composition from Zircaloy-2 only in having no nickel and a slightly greater iron content. Both variations are intended to reduce hydrogen pickup in reactor operation. The corrosion behavior of Zircaloy-4 is very similar to that of Zircaloy-2. However, hydrogen pickup for Zircaloy-4 is significantly lower, particularly when the alloy is exposed to water at 360 °F). At this temperature, hydrogen pickup for Zircaloy-4 is about 25% of theoretical, or less than half that for Zircaloy-2.

2.3.1.2 Surface Modification

Surface modification is the alternative to surface composition or structure by the use of high energy particle beams. Elements may be added to the surface to influence the surface characteristics of the substrate by the formation of alloys, metastable alloys or phases, or amorphous layers. Surface-modified layers are distinguished from conversion or coating layers by their greater similarity to metallurgical alloying versus chemically reacted, adhered, or physically bonded layers. However, surface structures are produced that differ significantly from those obtained by conventional metallurgical processes. This latter characteristic further distinguishes surface modification from other conventional processes, such as amalgamation or thermal diffusion. Two different modification methods will be discussed. The first, ion implantation, is the introduction of ionized species (usually elements, for example, Ti^+) into the substrate using kilovolt to megavolt ion accelerating potentials. The second method, laser processing, is high-power laser melting with or without mixing of materials precoated on the substrate, followed by rapid melt quenching.

The advantages of the surface modification approach to promoting corrosion resistance [45] include:

- Alteration of the surface without sacrifice of bulk properties
- Conservation of scarce, critical, or expensive alloying elements
- Production of novel surface alloys (unattainable by conventional metallurgical techniques) with superior properties
- Avoidance of coating adhesion problems because of no interface

The disadvantages of the surface modification techniques include:

- Processing materials having deep or hidden contours
- Cost of processing equipment
- Substrate sensitivity to high energy input (for example, thermal instability)
- The thinness (susceptibility to damage) of the coatings

Ion implantation. Surface modification by ion implantation is a technique that was derived from the semiconductor industry. Specimens for corrosion research were initially prepared by using high-energy research instrumentation or commercial semiconductor implanters. Equipment for surface modification of metal parts by batch processing has been built, and production capabilities of the equipment are being evaluated. Ion implantation is reaching a stage of development in which specific advantages are being recognized and exploited for enhancing the corrosion and wear resistance of critical metal parts [46].

The ion implantation technique consists of introducing the target (substrate material) into the implanter vacuum chamber, vaporizing and ionizing the implant species, and electrostatically accelerating the ionized species into the target.

The implant species can be most any element that can be vaporized and ionized in a vacuum chamber. Solid materials are heated to provide an adequate vapor pressure of the implant species. The vaporized material is ionized and accelerated toward the target. Magnetic fields separate various mass/charge ratios and enable the selection of specific implant species. A selected species impacts the target material and is implanted within, producing a surface-modified substrate. The depth to which the species is implanted depends on the accelerating voltage and the atomic numbers of the implant versus target species [47]. Commonly used acceleration voltages are 20 to 200 keV. The typical average implantation depth (range) is 10 to 100 nm. The distribution of implanted species versus range is roughly Gaussian.

There are some advantages of the ion implantation process [45]: Solid-solubility limit can be exceeded. Maximum concentrations of implanted species may be as high as 50 at.%. Depth concentration distribution and location are controllable, and composition can be changed without affecting grain sizes.

The implantation process can be viewed as a means of changing the material properties of an item only at the surface. An item can be fabricated from a material having desirable bulk properties (machinable, low-cost) and can be modified to provide the requisite surface properties (corrosion resistance, wearability).

There are two approaches to using ion implantation for increasing the corrosion resistance of substrates; the first is to enhance passivation characteristics, and the second is to create novel materials. In the first approach, implantation creates a surface composition based on conventional metallurgical experience that reacts to form a passive layer. In the second approach, implantation creates a surface composition and a structure that are difficult, impossible, or impractical to achieve by conventional metallurgy.

Substantial efforts have been made in the search for effective applications of ion implantation for enhancing corrosion resistance [48-52]. The greatest difficulty lies in the thinness of the implanted layer; corrosion-resistant layers must not be entirely consumed or damaged. Many research efforts have attempted to mimic conventional alloy compositions. However, the corrosion rates of conventional alloy systems are usually too high relative to the thinness of the implanted layer. The most successful approaches have involved detailed knowledge of a specific material and environmental corrosion conditions or have created unconventional materials.

Laser surface processing. Lasers with continuous outputs of 0.5 to 10 kW can be used to modify the metallurgical structure of a surface and to tailor the surface properties without adversely affecting the bulk properties. The surface modification can take the following three forms. The first is transformation hardening, in which a surface is heated so that thermal diffusion and solid-state transformations can take place [53, 54]. The second is surface melting, which results in a refinement of the structure due to the rapid quenching from the melt [53-56]. The third is surface alloying, in which alloying elements are added to the melt pool to change the composition of the surface [57-59]. The novel structures produced by laser surface melting and alloying can exhibit improved electrochemical behavior.

2.3.1.4 Overlay Coating by Vapor Deposition

Vapor-deposited coatings modify the surface properties of materials. They are widely used and have been particularly successful in improving such mechanical properties as wear, friction, and hardness in cutting applications. Their use as corrosion-resistant coatings is also becoming widespread.

The vapor deposition processes fall into two major categories--physical vapor deposition (PVD) and chemical vapor deposition (CVD)--which in turn comprise various subcategories.

The major deposition processes that will be reviewed in this thesis are sputtering, evaporation, ion plating, and CVD. These processes all have one characteristic in common: The deposition species are transferred and deposited in the form of individual atoms or molecules. In this respect, they are fundamentally different from particulate or liquid deposition processes, such as thermal spraying or electroplating

A primary benefit of vapor deposition is that it is essentially nondamaging to the environment, because there are no solvents or electrochemicals of which to dispose. At a time when environmental-protection regulations are continually being tightened, this crucial factor favors vapor deposition over other processes that may be more harmful to the environment.

Sputtering. Sputter deposition is the principal PVD process. It involves the transport of a material from a source (target) to a substrate by means of the bombardment of the target by gas ions that have been accelerated by a high voltage. Atoms from the target are ejected by momentum transfer between the incident ions and the target. These ejected particles move across the vacuum chamber to be deposited on the substrate.

Sputtering developed very rapidly in the 1970s in the semiconductor industry, in which the technique is essential for mass production. Sputtering is making rapid inroads in such corrosion applications as high-chromium alloy coatings on turbine blades and many other new applications that require high-quality coatings with good adhesion which can be further improved by sputter cleaning the substrate or by bias sputtering. Large equipment is readily available, and sputtering has become a highly automated process. The quality, structure, and uniformity of the deposit are excellent. However, it is a line-of-sight process that requires special fixtures and shaped targets to coat uniformly; furthermore, the coating of compound curves, recesses, and holes is difficult. It is also a high cost process.

Evaporation: the first PVD process used on an industrial basis for the aluminum metallization of plastics and glass for decorative purposes. Originally the most widely used process, evaporation has now been overtaken by sputtering.

The basic evaporation process involves the transfer of material to form a coating by physical means alone, essentially vaporization. Practically all metals can be evaporated, making evaporation a universal process with regard to metals. Unlike other vapor deposition processes, evaporation is a low-energy process, with particle energy averaging 0.2 to 0.3 eV as compared to 10 to 40 eV for sputtering, 200 eV or more for ion plating, and 100 keV for ion implantation. The term low energy means that adhesion of the particle to the substrate may be marginal. In addition, the temperature of the substrate is not increased by the deposition, which means there is little or no diffusion.

Very large evaporation equipment, which was developed for the optical industry, is commercially available. Coatings of several microns in thickness can be rapidly deposited. The disadvantages of this method are non-uniform coverage (limited to line of sight) and relatively low adhesion. Evaporation is very successful in applications in which adhesion and good structure are not critical, such as decorative and optical uses. Evaporation is not used for critical corrosion applications.

Ion plating: actually a hybrid concept based on the evaporation (or sputtering) mechanism coupled with a glow discharge. If the deposition species is ionized in a reactive gas, a compound is formed with some of the gas atoms, and deposition of the compound occurs. Ion plating is widely used and is gradually replacing pack cementation or diffusion.

The deposited species in ion plating have higher energy than those of evaporation or sputtering processes; this results in improved adhesion as well as a deposit with improved structure and fewer imperfections. On the negative side, the equipment is more complicated and therefore more expensive than either evaporation or sputtering equipment, and the process is more exacting. The level of ionization can be difficult to control, which may result in uneven deposition.

Chemical vapor deposition: a well-established deposition process that is extensively used in the semiconductor and cutting tool industries. It has the unique ability to deposit relatively thick, dense, high-quality films (up to 6.4 mm, or ¼ in. in thickness or more) at a cost that is generally, in case of thermal CVD, lower than that of PVD processes. The high temperature (about 1000 °C, or 1830 °F) necessary for CVD promotes good adhesion but also considerably restricts the type of substrate that can be coated to ceramics, refractory metals, and special alloys. To decrease the process temperature, other energy sources have been applied to the CVD process. Plasma assisted (PA) CVD and ultra violet (UV) CVD are the typical examples.

A constraint resulting from the high temperature of deposition is the stress in the deposit due to the difference in thermal expansion between substrate and deposit. These stresses may be sufficient to cause cracking, spalling, and loss of adhesion. The new technique of plasma CVD can be used at much lower temperatures in, for example, semiconductor applications, but the resulting films tend to incorporate impurities.

The materials that can be easily deposited by CVD are more limited than with PVD. Chemical vapor deposition is particularly useful for depositing compounds and refractory metals and lends itself very well to corrosion applications.

2.3.2 Metal/Ceramic Interfaces

Coating is an important technology due to the high demands placed on the capabilities and operative life of materials. However, the stresses, which are generated at the interface between a ceramic coating and a metal substrate, induced by the discontinuous character of the coating–substrate structure may generate cracks and the coating thus becomes very susceptible to spallation. The relatively high mismatch in thermal expansion coefficients causes a very high residual stresses, especially when the system is operated in a high-temperature environment, for example in the engine combustion chamber of an air vehicle or a nuclear fusion reaction container.

Metal/ceramic interfaces belong to hetero-phase boundaries. Those boundaries exist between two crystals that possess different structures and/or compositions. In contrast, a homo-phase boundary separates two crystals of the same material with the same composition (Figure 2.5).

Recently, heterophase boundaries and metal/ceramic interfaces were the subject of intense research. The great interest in metal/ceramic interfaces results from the high potential of application of those components: (i) for the bonding of metals to ceramics;

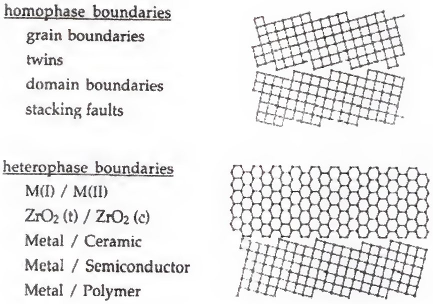

Figure 2.5. Homophase boundaries and heterophase boundaries.

(ii) as an important component of composites; (iii) electronic packaging systems used in information processing; (iv) thin film technology and (v) high-temperature oxidation of metals and metallic alloys. The metal/ceramic interfaces must typically sustain mechanical and/or electrical forces without failure. Consequently, interfaces exert an important, sometimes controlling influence on performance for the components mentioned above.

2.4 Requirements for Oxidation Protective Coating System

2.4.1 Coating Requirements

The desired characteristics for a protective oxide coating for cladding include the following:

- Corrosion and thermal resistant under pressurized water reactor conditions
- Smooth and uniform surfaces
- Good adherence to the metal substrate, which usually involves a coefficient of thermal expansion close to that of the metal, and sufficient high-temperature plasticity to resist fracture from differential thermal expansion stresses

- No diffusion pathways and micropores
- Low coefficient of diffusion of reactant species (metal cations, and corrodent anions) so that the oxide coating has a slow growth rate
- High thermodynamic stability (highly negative Gibbs free energy of formation) so that it re-forms preferentially to other possible reaction products
- Processing at low enough temperature to avoid changing underlying zirconium alloy structure (less than 600°C to prevent fatigue and 874 °C to prevent allotropic transformation of alpha (hcp) to beta (bcc))
- Moderate in cost & capability of treating full length (14 feet) tubes
- No adverse effects upon nucleonics

2.4.2 Material Selection

Our research group has investigated several materials to identify ceramics that could be used as a protective coating [35]. The chosen ceramics are the following: alumina, boron carbide, graphite, mullite, silicon carbide, spinel, tungsten carbide, zirconia, and zirconium carbide. Their mechanical properties, such as coefficient of thermal expansion (CTE) and thermal conductivity, were compared with that of zirconium to determine the best candidate. The hydrothermal stability and the thermal neutron cross section of the candidate materials were also considered to determine the best candidate. Certain ceramic information, such as hardness, availability, and chemical stability, eliminated some of the options early. The ceramics that seemed most likely as coating choices were alumina and silicon carbide. An extremely important parameter was the thermal expansion coefficient. In this case, alumina is within 12% of zirconium's CTE and would be the best choice for these criteria. For thermal conductivity and thermal flux, the coating less than 50 microns did not cause significant increases in the temperatures in any of the regions inside the cladding. At a maximum suitable coating thickness of 50 microns, alumina would cause a 0.45% drop in the thermal flux in the fuel and 1.7% drop in the thermal flux in the water, which would only cause a 0.031% increase in the cladding temperature and 0.011% increase in the fuel centerline temperature. Alumina also has a low enough thermal neutron cross section and been reported for its hydrothermal stability.

2.5 Aluminum Oxide Coatings

Alumina (Al_2O_3) is one of the most commonly used materials in the production of ceramics. Alumina has a wide acceptance due to its high hardness, and its excellent wear and corrosion resistance. Current uses for alumina include the following:

- Substrate materials in electronics
- Translucent envelopes for sodium-vapor lamps
- Cutting tool inserts
- Water faucet valves
- Pump components

The microstructure and resulting properties of alumina ceramics are strongly dependent on the percentage of alumina present. Generally, the higher the concentration of alumina: the more simple the grain structure, the higher the hardness, and the higher the thermal conductivity. Because of strong chemical bond strength between the aluminum and oxygen ions, alumina has outstanding physical stability. It has a melting point of 2050°C, the highest hardness among oxides, and a high mechanical strength. Its thermal conductivity is average among oxides. It does have a large coefficient of thermal expansion that is lower than silicon carbide, but alumina almost matches the thermal expansion of zirconium. Alumina is also chemically very stable and has high corrosion resistance. Studies have shown alumina to be not soluble in water of the temperature and pH utilized in light water reactors [60]. Alumina is a prime candidate as a coating material for Zircaloy cladding.

A number of transitional Al_2O_3 structures can form initially with increasing temperatures, but all structures are transformed irreversibly to α-Al_2O_3 with a corundum structure of a hexagonal system. α-Al_2O_3, the only stable form above 1200°C (2190°F), is generally used for structural and electrical applications, except for γ-Al_2O_3, which is used for catalytic application.

2.5.1 Properties of Alumina Coatings

Alumina is a technologically attractive ceramic material because of its excellent properties such as high hardness and wear resistance, high chemical stability, and good electrical resistivity as mentioned above.

Aluminum oxide (Al_2O_3) as a coating has many attractive properties such as relatively low volatility, low O_2 diffusion coefficients, slow growth kinetics, excellent high temperature strength, good corrosion resistance and oxidation stability. Al_2O_3 coatings have been widely prepared by vacuum methods, i.e. physical vapor deposition (PVD) and chemical vapor deposition (CVD), because of their versatile applications in engineering. Thin Al_2O_3 coatings prepared by PVD methods are used for optical filters, microelectronics, insulating coatings on Cu electrodes and insulator modules in channels of magneto-hydrodynamic generators.

For nuclear industry, the properties of alumina including high corrosion resistance, plus low thermal neutron cross section, high thermal conductivity, low mismatch of coefficient of thermal expansion (CTE) with Zircaloy make alumina the strongest candidate materials for nuclear reactor applications.

2.5.2 Alumina in Sub-Critical Aqueous Conditions

Alumina is known to be corrosion resistant in corrosive aqueous solutions at elevated temperatures [61]. No intercrystalline corrosion was found on high-purity alumina (>99.9% Al_2O_3) [61]. All investigations showed that the corrosion resistance of alumina ceramics is influenced by the purity of the materials due to a segregation of impurities to the grain boundaries.

Intergranular corrosion proceeded in the alumina ceramics by preferential attack at the grain boundaries. After dissolution of the grain boundary phase, the grains are completely exposed to the corrosive medium and are finally washed out. Furthermore, the porosity and the microstructure of the ceramic material are important for the corrosion resistance. Al_2O_3 ceramics with closed porosity and large grain sizes are more resistant to corrosive attack.

The corrosion of alumina ceramics in aqueous solutions is determined by the solubility of alumina and the solubilities of the corrosion products are of crucial importance for the corrosion resistance of the aluminas.

Boehmite (AlOOH) was formed at the surface of 99% alumina by hydrothermal reaction at 300°C for 10d. The more impurities and longer time, the more dissolution of Al_2O_3 and formation of AlOOH. The form of the hydrothermal corrosion in Al_2O_3 ceramics can be categorized as intergranular corrosion.

However, there have been no reports about amorphous or metastable transition aluminas especially as a form of thin films under subcritical condition.

2.5.3 Phase Transformation and Temperature Dependence of Aluminum Oxide

Alumina can exist in a number of metastable polymorphs in addition to the thermodynamically stable α-alumina which crystallizes in a rhombohedral structure, with can be described as O^{2-} ions in an approximately hexagonal closed packed arrangement and Al^{3+} ions occupying two-thirds of the octahedral interstices. Other alumina phases frequently observed in PVD coatings are cubic γ-alumina, tetragonal δ- and monoclinic θ-alumina. Table 2-3 gives the microstructures of Al_2O_3 films obtained by various methods and their thermal annealing behaviors. The CVD formation of α-, κ-, and θ-alumina has been reported[64, 65]. All metastable phases transform irreversibly to α-alumina at sufficiently high temperatures. Since this phase transformation is associated with a volume change of the unit cell, it can result in catastrophic failure of the coating.

Table 2.3. Structures and annealing behaviors of Al2O3 films synthesized by various PVD methods [16, 62, 63]

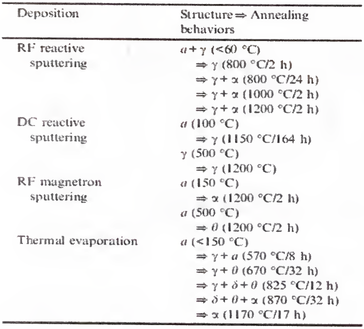

Deposition	Structure ⇒ Annealing behaviors
RF reactive sputtering	$a+\gamma$ (<60 °C) ⇒ γ (800 °C/2 h) ⇒ $\gamma+\alpha$ (800 °C/24 h) ⇒ $\gamma+\alpha$ (1000 °C/2 h) ⇒ $\gamma+\alpha$ (1200 °C/2 h)
DC reactive sputtering	a (100 °C) ⇒ γ (1150 °C/164 h) γ (500 °C) ⇒ γ (1200 °C)
RF magnetron sputtering	a (150 °C) ⇒ α (1200 °C/2 h) a (500 °C) ⇒ θ (1200 °C/2 h)
Thermal evaporation	a (<150 °C) ⇒ $\gamma+a$ (570 °C/8 h) ⇒ $\gamma+\theta$ (670 °C/32 h) ⇒ $\gamma+\delta+\theta$ (825 °C/12 h) ⇒ $\delta+\theta+\alpha$ (870 °C/32 h) ⇒ α (1170 °C/17 h)

2.6 Compositional Gradient Coatings

2.6.1 Concept

Coating is an important technology due to the high demands placed on the capabilities and operative life of materials. However, the stresses, which are generated at the interface between a ceramic coating and a metal substrate, induced by the discontinuous character of the coating–substrate structure may generate cracks and the coating thus becomes very susceptible to spallation. The relatively high mismatch in thermal expansion coefficients causes a very high residual stresses, especially when the system is operated in a high-temperature environment, for example in the engine combustion chamber of an air vehicle or a nuclear fusion reaction container.

The introduction of interlayer at ceramic/metal interface has been the most popular method to increase the adhesion property and minimize the failure between metal and ceramic. However, in nuclear applications material selection is the major issue to consider since nuclear related properties, such as thermal neutron absorption cross-section especially, are in the highest priority, although other properties are necessary and promising in material selection. Therefore, introduction of another material such as interlayer to the system can make many variables by itself. Furthermore, it is hard to select proper materials satisfying the requirements of nuclear as well as other properties.

Therefore, instead of addition of interlayer, compositional gradient structure using the existent materials in the system must be the most appropriate way. Generally, compositional gradient structure is included in so-called functionally gradient materials (FGM). In other words, FGM is the sort of standarized term.

The term functionally graded material (FGM) describes a two-phase material where the volume fraction of the second phase increases across the thickness of the material in a gradient which may be continuous or stepwise [66]. Continuous gradients have a smooth transitional gradient across the microstructure, whereas stepped gradients are characterised by abrupt changes in composition arising from the limitations of the manufacturing route.

In FGMs, the graded changes in composition and microstructure can reduce or eliminate specific interfaces between constituent materials such as ceramics and metals. In other words, the aim of production of FGMs is eliminating the macroscopic boundary in materials in which the material's mechanical, physical and chemical properties change continuously and which have no discontinuities within the material.

Functional graded materials (FGMs) are also ideal to combine the incompatible properties of heat resistance and strength with low internal stress, by producing a compositional gradient structure of distinct ceramic and metal phases [67].

The introduction of the functionally graded materials (FGM) concept to a coating design is aimed at achieving improvements of reliability and longevity. The idea of FGM was substantially pushed in the early 1980s in Japan, where this new material concept was proposed to increase adhesion and minimize the thermal stresses in metallic–ceramic composites being developed for reusable rocket engines [68].

The concept of the so-called functionally graded material (FGM) has been introduced to eliminate singular stresses, relax residual stresses, and enhance bonding strength [69]. The graded material can be formed by continuously varying the constituent of multi-phase materials in a predetermined profile to produce an FGM [70-72] or by piecewise changing the material to result in a multi-layered medium. Consequently, in an FGM, the interfaces between two materials disappear but the characteristics of two or more different materials of the composite are preserved. Studies of FGMs reveal that the thermal residual stresses can be effectively relaxed by using an FGM coating in a coating–substrate system [73-75].

In coatings and thin structures, compositions of multiple phases are varied along the thickness direction. This graded feature is essential to achieve required functions to through preventing the material failure.

The graded coating must be designed and processed in a manner that prevents its delamination and spallation during thermal loading in service conditions.

2.6.2 Processes and Applications

A wide range of processes such as physical vapor deposition (PVD), chemical vapor deposition (CVD), plasma spraying, arc spraying, pulsed laser deposition (PLD), sol–gel techniques, common powder metallurgy, as well as build-up welding have been reported for FGM production [76, 77].

When the concept of FGMs was first proposed in 1984 it was a response to the need for materials which could serve as thermal barriers while developing low residual stresses. FGM concepts have been applied to metals, ceramics and organic composites to generate improved components with superior physical properties [78, 79]. Graded coating designs are used mainly for protection of metallic or ceramic substrates against oxidation, heat penetration, wear and corrosion. While the first two requirements are aimed at improving high-temperature capabilities, the latter deal with the deposition of extremely hard coatings on heavy duty components such as cutting tools to increase wear resistance, and with embedding hardening alloying elements or hard particles into light alloys to improve their corrosion resistance. Depending on the application and the specific loading conditions, varying approaches to generate the gradients must be followed.

The FGM concept can also be applied to various materials for structural uses, based on the integration of incompatible functions such as the refractoriness of ceramics and the toughness of metals, and for functional applications—the direct conversion of thermal energy to electric energy—as well as to produce multifunctional devices.[80]

Another common application of FGMs is in the field of electroceramics, as actuators and carriers of energy conservation devices. In optics, FGMs can be used to produce fibers with a smoothly varying refractive index.

A large variety of functional effects draw advantage from the FGM principle, such as graded thermoelectrics and dielectrics (e.g. thin films prepared by chemical solution deposition [81], piezoelectrically graded materials, applied for broadband ultrasonic transducers [82], and graded composite electrodes for solid oxide fuel cells (SOFC) [83]. Moreover, functional applications comprise tungsten–copper composites for high current connectors [84, 85] and divertor plates [82], electrodes for thermionics [86], photocatalysts, advanced superconducting wires, optical polymers, magnetic properties, liquid crystals, single crystals with tuned lattice constant for X-ray monochromators, electronic high mobility In–Sb alloys, photonic crystals, and refraction graded optical multilayers [82, 86, 87]. Aerospace application of graded structures has also been surveyed [88].

2.6.3 Issues on Functionally Graded Materials (FGMs)

Disadvantages of single layer coating have been able to be overcome by multi-layer coatings. The multi-layered coatings that are comprised of dissimilar homogeneous materials have stress singularities at the intersection of an interface and a free surface [89]. The use of more layers in a multi-layered medium weakens the stress singularity, implying reducing stress intensity factors (SIFs). The comparison of the stress behavior of an FGM coating with those of a multi-layered coating bonded to a metal substrate due to a uniform temperature change, as investigated by Lee and Erdogan [90], indicated that the stress concentrations in the FGM-coated medium are less than those in the multi-layered homogeneous coating.

The fabrication process of FGMs is a quite complex task. In this sense, most published works deal with laminated samples that are formed by homogeneous layers of different compositions. However, continuous FGMs are scarcely reported. An extraordinary effort has been made in order to develop continuous FGMs in a wide range of systems and it has been attained in several works.

CHAPTER 3
EXPERIMENTAL

3.1 Introduction

This chapter describes the Zircaloy-4 samples used for the experiments with their composition, polishing and cleaning procedure that are followed by coating processes, heat treatment and characterizations. The coating processes consist of the RF magnetron sputter deposition system and electron beam evaporation system. After the thin film deposition step, the samples were heat treated in an tube furnace. Then the samples were characterized for their microstructure, elemental composition, mechanical properties, hydrothermal stability and interfacial reaction products.

3.2 Substrate Material

Zirconium alloy (Zircaloy-4) samples, with chemical composition given in Table 3.1., were used as substrates. Zircaloy-4 substrates were obtained as sheet stock from Western Zirconium (Odgen, Utah, USA). The alloy was vacuum arc re-melted (VAR) to an ingot, which was then broken down and rolled to sheet. Generally these alloys are rolled at high temperature in the beta region, then solution treated at about 1065°C (1950°F) and water quenched. Subsequent hot working and heat treating is done in the alpha region (below 790°C) to preserve the fine, uniform distribution of intermetallic compounds that result from solution treating and quenching. The sheet was rolled to a thickness of 1.6 mm (0.063") and was sheared into sizes of 9.5 cm x 30 cm (3.75" x 12"). Rectangular (1 cm x 1 cm) and circular (5/8" diameter) specimens were cut from the sheet. Substrates were polished with up to 600 grit paper, which is the polishing limit for commercial application. Polished surfaces were generally ultrasonically cleaned for 5 minutes to remove debris and then rinsed in methanol.

Table 3.1. Chemical composition of Zircaloy-4.

Sn	Fe	Cr	Si	C	O	Zr
1.37	0.2	0.11	0.01	0.014	0.124	Bal.

3.3 Coating Processes

Amorphous aluminum oxide coatings were deposited by RF magnetron sputtering system. Aluminum metal depositions to make the compositional gradient layers were performed by electron beam evaporation system.

3.3.1 Alumina ceramic coating by RF magnetron sputtering system

Sputtered alumina coatings were made using a custom built RF magnetron sputtering system. An illustration of the system's bell jar and geometry of the sources and substrate holder are shown in Figure 3.1 with an actual picture. This system has a RF planar magnetron sources configured in a sputter up geometry. The power source is manufactured by US Guns Inc, is designed for a 2” (5 cm) target diameter. The RF supply includes a RF Plasma Products model RF-5 generator with an automatic impedance matching network. The substrate support has integrated temperature control utilizing resistive Watlow cartridge heating elements and a thermocouple. The vacuum necessary for sputtering is generated inside a Varian stainless steel bell jar and base plate style chamber. A turbo pump and rotary vane pump (Sargent-Welch model 1397) provide the high vacuum and rough pumping, respectively. A throttle valve is between the system and the turbo pump. This system has two MFCs for Ar and O_2, which are used as sputtering gas and reactive gas, respectively, in the system. Vacuum gauging consists of one ionization gauge, two thermocouple gauges, and one Baratron gauge.

The base pressure was $4\text{x}10^{-3}$ Pa ($3\text{x}10^{-5}$ torr) and the operating pressure was 0.67 Pa ($5\ \text{x}10^{-3}$ torr). Argon flow was 15 sccm and the RF power was 100W. Coatings were deposited at room temperature for 2 hours with a target-substrate distance of 7.6 cm (3 inches).

3.3.2 Aluminum metal deposition by electron beam evaporation

Aluminum metal films to make compositional gradient layers were deposited in an electron beam evaporation system with a glass bell jar. Electron beam evaporation provides fast and easy deposition as compared to sputter deposition. Deposition of high melting point elements can be performed more easily with electron beam evaporation than from thermal evaporation sources. The electron beam evaporation system used for this research was pumped with a Varian oil diffusion pump backed by a two-stage mechanical rotary vane pump, providing a base pressure of $1\times10^{-6} \sim 2\times10^{-6}$ torr. A schematic of the electron beam evaporation system is shown in Figure 3.2.

The source aluminum metal in the electron beam well consisted of metal pellet with a purity of 99.95% (Cerac). The thickness of the deposited metal layers was monitored using a quartz crystal oscillator that was installed next to the sample stage.

For aluminum deposition in this case, the base pressure was 9×10^{-7} Torr and the operating pressure was 5×10^{-5} Torr with a power of 4.5 kV. Coatings were deposited at room temperature with a target-substrate distance of 370 mm. The deposition rate was 100 nm/min.

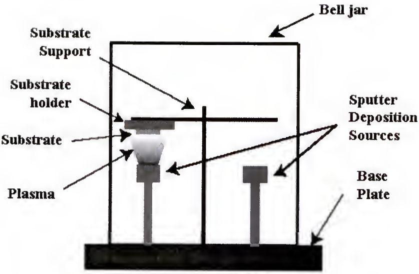

(a)

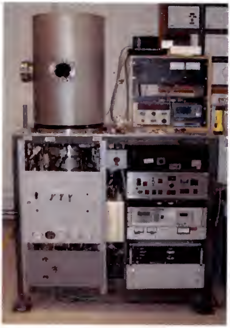

(b)

Figure 3.1. (a) Schematic diagram of cross-sectional view and (b) picture of the sputter deposition system

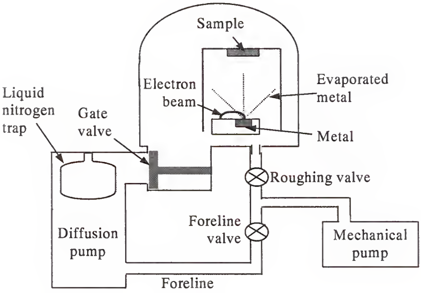

Figure 3.2. Schematic of the electron beam evaporation system

3.3 Heat Treatments

Coated samples were annealed using tube furnace (Lindberg/Blue TF55030) in the flowing air atmosphere. Sputter-deposited samples were annealed at various temperatures to investigate the influence of annealing on the film structure and properties. To make the compositional gradient layers aluminum metal films on Zircaloy deposited by electron beam evaporation were annealed in tube furnace in air. Samples were annealed at temperatures of 500℃ for two hours. Annealing using a two-step heating schedule was also used, where samples were held at 650℃ for 30 minutes and 500℃ for 2 hours.

3.4 Coating Characterizations

Surface and layer composition, surface and interfacial morphology and structure, and interfacial reaction products were characterized using the following physical characterization techniques.

Stylus profilometer was used to measure the thickness of the films and to brief check the cross section of surface topography of polished substrates. To measure thickness of the deposited films, a portion of the Si substrate was masked with aluminum foil. After the deposition, the foil was removed yielding a well defined step. A Tencor alpha-step 500 surface profiler was used to measure the height of the step, and therefore the film thickness.

The Zircaloy-4 substrates and the applied ceramic coatings before and after autoclave exposure were examined using scanning electron microscopy (JOEL JSM 6400) as well as high-resolution secondary electron microscopy (JEOL 6335F), which provided highly magnified topographical images of the surface. This allowed the detection of microcracks in the coatings with a resolution of a few nanometers. Energy-dispersive x-ray spectroscopy (EDS) was used to obtain compositional information of the sample surfaces.

Auger electron spectroscopy (AES)[91, 92] was used to determine the various elements present at the surface of the samples. The surface was bombarded with a 10 keV electron beam. The electrons create inner quantum shell vacancies, which are filled with an electron decaying from a higher shell. The energy difference between these two levels is transferred to and causes ejection of another electron, the Auger electron. The Auger has a specific energy characteristic of the element. Due to energy loss, Auger electrons originating deeper than 3~4 atomic layers in the solid (5~20Å) are inelastically scattered before reaching the surface and therefore can not be used for elemental identification. In this study, AES data were obtained from a Perkin-Elmer PHI 660 Scanning Auger Electron Multi probe in the N (E) mode. The primary energy used was 10 kV with a current of 100nA. AES may be combined with ion sputtering to clean the surface as well as perform depth analysis [92]. The Auger electron intensities are plotted as a function of the sputtering time. The relative intensity changes give compositional information as a function of depth. Ar+ was used to sputter the surface for depth profile. Quantification of elemental concentrations in AES data is possible in cases where sensitivity factors have been measured in the same sample matrix [91, 92]. The following equation is used for the calculation of elemental concentrations.

$$C_E(\%) = 100\% \times \frac{I_E / S_E}{\sum_X I_X / S_X} \tag{3.1}$$

where I_E is analyte intensity, S_E is analyte sensitivity factor, I_X is intensity of other elements, and S_X is sensitivity factor of other elements in the samples.

X-ray diffraction (XRD)[92] was used to identify the phases formed at the contacts. A collimated beam of X-rays is incident on a specimen and is diffracted by the crystalline phases in the specimen according to Bragg's law ($\lambda = 2d \sin\theta$, where d is the spacing between atomic planes in the crystalline phase). The intensity of the diffracted X-ray beam is measured as a function of the diffraction angle, 2θ, and the specimen's orientation. The time evolution of the interfacial phases was also studied as a function of annealing condition. Since some coatings of the films used in this study were relatively thin (100 to 300 nm), a glancing angle (1°) X-ray diffraction technique was employed to get enough X-ray intensities from the sample. The XRD data was obtained from a Phillips Model: PANalytical Hybrid X'pert MRD system with a Cu $K_{\alpha\&\beta}$ averaged source.

Transmission electron microscopy (TEM)[92] was used to identify the phases, their distribution and microstructure formed in the coatings. A thin solid specimen is bombarded in vacuum with a highly focused, mono energetic beam of electrons. The beam is of sufficient energy (200kV) to propagate through the specimen. A series of electromagnetic lenses magnify this transmitted electron signal. Diffracted electrons can be used to form a diffraction pattern to determine the atomic structure of the material. Transmitted electrons can be used to form images from small regions of the sample, due to several scattering mechanisms associated with interactions between electrons and the atomic constituents of the sample. A high resolution TEM system (JEOL JEM 2010F Field Emission Microscope) was used for this study. In-situ EDS system was used to investigate the compositional distribution through the sample and to get the compositional line scan along the thickness. For TEM sample preparation, a focused ion beam (FIB, Model: FEI 210) technique was employed [92]. FIB TEM specimens prepared by the "lift-out" method provide a rapid means of preparing an electron transparent cross-section from a specific site of interest. A sample is inserted directly into the FIB chamber and a specimen created straight from the samples' surface. Two trenches were milled on either side of the site of interest, the area in the middle was thinned until it was electron transparent, and then the cross-section was cut free by the FIB. The specimen was then "lifted out" by the use of an electrostatic probe, which retrieved the free sample from its trench and deposited it on a TEM grid that was made up of copper covered with carbon thin films.

The nature of atomic bonds in coatings materials was investigated using x-ray photoelectron spectroscopy (XPS). XPS spectra were taken on a PHI model 5100 ESCA system. A non-monochromated Mg Kα X-ray source, producing characteristic radiation with a peak photon energy at 1253.6 eV was used for all spectra. The X-ray generator was operated at 15 kV and 300 watts (20 mA). Photoelectrons liberated from the sample are collected, retarded, and analyzed in a hemispherical analyzer. The analyzer acts as a band pass filter, allowing only electrons with a particular kinetic energy through to the Channeltron detector. The kinetic energy is converted into binding energy through use of Equation 3.2:

$$BE = h\nu - KE - \phi_D \qquad (3.2)$$

where BE is the binding energy of the detected electron, h is Planck's constant, ν is the frequency of X-ray probe beam, KE is the kinetic energy of the photoelectron, and ϕD (4.7 eV) is the work function of the detector (hemispherical analyzer). Spectra are traditionally presented starting with the highest binding energy to the lowest on the abscissa. Similar to AES, XPS is also a surface analysis techniques due to the limited escape depth of measured photoelectrons.

Surface morphology and roughness are characterized by atomic force microscopy (Digital Instruments Nanoscope III) in the continuous mode. When the tip comes within the AFM in which a sharp tip is mounted on a flexible cantilever. When the tip comes within a few Å of the sample's surface, repulsive van der Waals forces between the atoms on the tip and those on the sample cause the cantilever to deflect. The magnitude of the deflection depends on the tip-to-sample distance d. The most common method for monitoring the deflection is with the beam bounce detection system. In this system, light from a laser is reflected from the back of the cantilever onto a position-sensitive photodiode. A given cantilever deflection corresponds to a specific position of the laser beam on the position-sensitive photodiode. The position-sensitive photodiode can detect about 0.1Å displacements.

Hardness and modulus of elasticity of the deposited alumina films were determined by the Hystron nanoindetoation machine (TriboIndentor) using Berkovich tip. Repeated indentations of 30 points were performed, and the average value of the hardness and modulus was obtained. SiO_2/Si substrates were used since the roughness of actual polished Zircaloy substrate was too high to perform the nano-scale indentation. To avoid the substrate effect the indentation depth was limited to 1/10 of the film thickness as suggested by ASTM. In the instrument, software uses a standard routine based on the unloading stiffness of the force displacement data to calculate the hardness and modulus values.

Tip-shape calibration is based on determingin the area function of the indenter tip. The method is based on the assumption that Young's modulus of elasticity is constant and endependent of indentation depth. As area function relating the projected contact area (A) to the contact depth (hc) is obtained. For an ideal pyramidal geometry tip (Berkovich), the projected contact area to depthe relationship is given by

$$A = 24.5\ h_c^2 \qquad (3.3)$$

The initial umloading contact stiffness, S = (dP/dh) ie. the slope of the initial portion of the unloading curve is given by

$$S = \frac{dP}{dh} = \frac{2}{\sqrt{\pi}} E_r \sqrt{A} \qquad (3.4)$$

Rearranging eq.(3.4) we get

$$A = \frac{\pi}{4}\left(\frac{S}{E_r}\right)^2 \qquad (3.5)$$

where the reduced modulus E_r accounts for the fact that the measured displacement includes contribution from both the specimen and the indenter. The reduced modulus is given by

$$\frac{1}{E_r} = \left(\frac{1-\nu^2}{E}\right)_{specimen} + \left(\frac{1-\nu^2}{E}\right)_{indenter} \tag{3.6}$$

where E and ν are the elastic modulus and Poisson's ratio of the specimen and the indenter respectively. The hardness has the normal definition

$$H = \frac{P_{\max}}{A} \tag{3.7}$$

where P_{max} is the maximum indentation force and A is the resultant projected contact area at that load. To determine the area function, a series of indents at various contact depths (normal loads) are performed on fused quartz specimen and the contact area (A) calculated using eq (3.5).

To investigate the adhesion property, a nano scratch tester at Micro-photonics in California was employed. The scratch test method consists of the generation of scratches with a spherical stylus (Rockwell C diamond, tip radius 5 μm), which is drawn at a constant speed across the coating substrate system to be tested, under progressive loading at a fixed rate. The critical load (L_c) is defined as the smallest load at which a recognizable failure occurs. The diagram (Figure 3.3) shows the fundamental components of the Nano-Scratch Tester. The stylus is mounted on a double cantilever beam in order to maintain the indenter in a vertical plane during measurement, to reduce the torsional effects during scratching and to increase accuracy. Different double cantilever configurations can be mounted on the measuring head to provide maximum applied load ranges of 10mN, 100mN and 1N with respective resolutions of 0.15, 1.5 and configurations can be mounted on the measuring head to provide maximum applied load ranges of 10mN, 100mN and 1N with respective resolutions of 0.15, 1.5 and 15μN. The load is applied by a displacement actuator that consists of an electromagnetic cell coupled with a piezoelectric nanopositioning device. The latter provides a very fast response time for the normal load feedback control loop and gives greatly improved load application. The displacement sensor, D_z, monitors the surface profile of the sample under a constant load. This is a very useful method of measuring the penetration depth during a scratching operation and the residual depth after a scratch test has been completed. The displacement sensor, F_N, measures the deflection of the double cantilever beam and consists of a linear voltage differential transformer (LVDT). An adjustable feedback

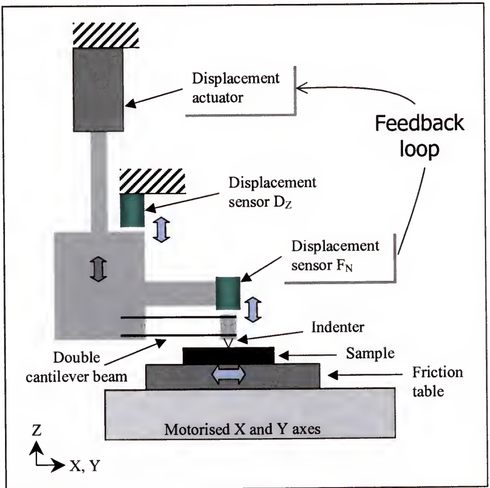

system allows the applied load to be maintained at the desired value. The sample is mounted on a friction table, which permits frictional variations to be characterized during a scratch test. The motorized X and Y axes allow the sample to be positioned with a lateral resolution of 1µm, this being particularly useful for localized measurements.

The scratch test is basically a comparison test. The critical loads depend, of course, on the mechanical strength (adhesion, cohesion) of a coating substrate composite but also on several other parameters: some of them are directly related to the test itself, while others are related to the coating-substrate system [93]. The test specific parameters include loading rate, scratching speed, indenter tip radius, indenter material and also tip wear. The coating-substrate specific parameters include substrate hardness and roughness, coating thickness and roughness, friction coefficient between coating and indenter and internal stresses in the coating. The test parameters, which have been used to investigate the effect of compositional gradient interlayer, are shown in Table 3.2.

Table 3.2. Test conditions for scratch analysis of samples

	Without FGM	With FGM
Load Type	Progressive	Progressive
Initial Load	1 mN	1 mN
Final Load	75 mN	350 mN
Loading Rate	75 mN/min	100 mN/min
Scratch Length	2 mm	7 mm
Speed	2 mm/min	2 mm/min
Scanning Load	N/A	N/A
Cantilever	ST-020	HL-101
Indenter	Rockwell 5 µm Diamond BA28745	Rockwell 5 µm Diamond BA28745

Samples were exposed to hydrothermal conditions in an autoclave (manufactured by Autoclave Engineers) at 20.1 MPa (3000 psi) and 343°C (650°F) for 24 hours and characterized to investigate phenomena under actual operating conditions of the cladding

Samples were exposed to hydrothermal conditions in an autoclave (manufactured by Autoclave Engineers) at 20.1 MPa (3000 psi) and 343°C (650°F) for 24 hours and characterized to investigate phenomena under actual operating conditions of the cladding in a light water reactor. The autoclave is a high pressure, high temperature system used to simulate the conditions experienced by Zircaloy cladding inside a light water reactor. (The autoclave system used in the experiments, shown in figure 3.4 basically consists of a high pressure vessel made of 316SS, electric resistance heater, seal system, pressure regulator, safety head valve to control the pressure and thermocouple for temperature control. The sample holder is made of Zircaloy to prevent the formation byproducts.

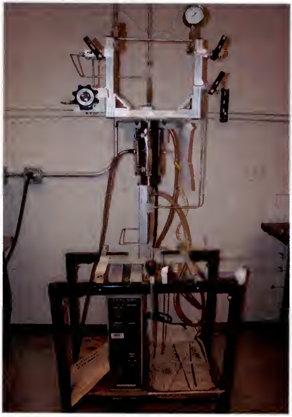

Figure 3.4. The picture of autoclave system used for hydrothermal testing

CHAPTER 4
PROPERTIES OF AMORPHOUS ALUMINA THIN FILMS

4.1 Introduction

The utility of thin ceramic films to serve as corrosion barriers has often been compromised by film defects, which are commonly attributed to film defects that allow the atmosphere reach the underlying material or that enhance the corrosion process.

It has been reported that amorphous oxide coatings are more corrosion resistant than polycrystalline oxides since the amorphous oxide layer is free of grain boundaries, particles and segregation [94]. The absence of those crystalline defects makes the electrochemical breakdown of amorphous oxide film difficult. These important features can prevent the penetration of oxidants.

Therefore, we propose an amorphous alumina oxide film for corrosion protection system for Zircaloy cladding in pressurized water reactor (PWR). To establish the system for actual application, the properties of the coating system need to be investigated. For example, the defects of micro- and macro- structure in the coating system should be concerned. Especially, since the properties of the thin films can be affected by heat treatment, the influence of the heat treatment on the microstructure and properties of the films will be discussed.

4.2 Annealing Temperature Dependence and Thermal Stability

Thin films deposited at a substrate temperature below the crystallization temperature of the thin films are amorphous. The metals generally show low crystallization temperature, however compounds such as oxides typically are much higher. The crystallization temperature of alumina is 1003°K (730°C) [95]for γ-alumina, one of the transition aluminas. Therefore, alumina films deposited at temperature lower than 730°C should be amorphous unless other energy source besides thermal energy is applied.

After a film has been deposited, it may be treated to further increase its functionality. Heat treatment is one of the most popular processing among the post deposition processings. Post-deposition heating can create film stresses due to differences in the coefficient of thermal expansion between the film and substrate and between different phases in the film. These stresses can result in plastic deformation of the film or substrate materials [96], create stress-related changes in the film properties, or create interfacial fracture.

However, post-deposition heat treatment is also used to promote mass transport (diffusion) so as to anneal the residual stress and defect structure in deposited films. Heating can be used to induce grain growth or phase changes [97, 98]. The substrate material and structure can influence the kinetics of the phase change by influencing the nucleation the new phase. However, post-deposition heating rarely allows densification of columnar films because surface layer formation at ambient prevents the diffusion needed for densification.

Post heat treatment can promote reaction of the deposited material with an ambient gas on the surface. Post-deposition diffusion and reaction can form a more extensive interfacial region and induce compound formation, and it alloy the deposited materials with the substrate surface [99, 100]. Post-deposition heating and diffusion can be used to completely convert the deposited material to interfacial material [99, 100].

In this chapter, the influence of annealing on coating structure, morphology and mechanical properties will be discussed.

4.2.1 Microstructure Of Sputter Deposited Alumina Films On Zircaloy

Although the temperature of our interest is equal to or less than 600°C because the cladding is maintained at less than 600°C associated with the reactor operation temperature and structure change in the Zircaloy substrate [101, 102]. Sputter deposited amorphous alumina coatings were, however, annealed in air at temperatures of 350°C, 450°C, 550°C, 650°C, 800°C, 1000°C and 1200°C to investigate the film characteristics and substrate structural changes over a wide range of temperatures.

The coatings annealed below 550°C showed no change in XRD diffraction patterns. The coatings annealed above 1000°C completely peeled off due to the failure induced by the volume change due to the allotropical transformation of ZrO_2 at 870°C.

The selected X-ray diffraction patterns of the alumina thin films on Zircaloy using RF magnetron sputter deposition are shown in figure 4.1. The diffraction patterns of the coatings annealed up to 500°C show the same pattern as the as-deposited coating, suggesting that the film structures annealed below 500°C are amorphous. These results are in agreement with the results reported in the literature [16, 62, 63]. Above the temperature of 550°C, Zr_3O and ZrO_2 peaks appeared. This was due to the penetration of oxygen from annealing ambient through the coating and the reaction of oxygen with the substrate. Because the coating structure of sputter deposited film at low temperature is generally a columnar structure, oxygen can penetrate through the coating along the column boundary or porosity between the columns. With increasing temperature, when the diffusion coefficient of oxygen in aluminum oxide reaches the critical point where

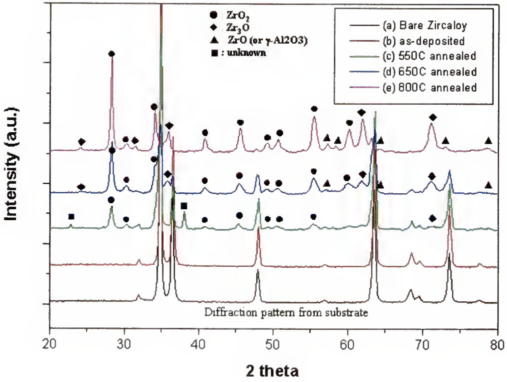

Figure 4.1. XRD spectrum of (a) Zircaloy substrate only, (b) as-deposited, (c) 550°C annealed (d) 650°C annealed and (e) 800°C annealed Al_2O_3 coatings on Zircaloy substrates, using RF magnetron sputtering. Annealing was performed in air for 2 hours.

enough oxygen gets through the coating during the annealing time of 2 hours, zirconium could react with oxygen to form zirconium oxide.

It was reported that amorphous alumina could be converted to transition metastable γ-alumina at around 650°C [16, 62, 63]. Since some zirconium oxide peaks in the XRD spectrum in Figure4.1 overlapped with γ-alumina peaks, it was difficult to identify the γ-alumina peaks.

The small peaks that existed in a coated sample and main peaks of zirconium disappeared in the uncoated sample because the growing zirconium oxides reduces the detection of the amount of the diffracted x-ray for the small peaks.

Thermal Stability. In the previous discussions the formation of zirconium oxide and the change of surface morphology in the structure of the amorphous alumina coated Zircaloy system above 550°C were reported. However, it can be concluded that amorphous alumina coated Zircaloy remained up to 500°C suggesting that the coating system had been thermally stable under those conditions.

Figure 4-2 is the XRD spectrum of an uncoated Zircaloy substrate annealed at 500°C for 2 hours and that of an amorphous alumina coated Zircaloy annealed at 500°C for 2 hours. This result showed that amorphous alumina played a role to prevent the penetration of oxygen from reacting with substrate up to 500°C. However, it was observed that XRD spectrum of the amorphous alumina coated Zircaloy was similar to that of the uncoated Zircaloy above 550°C. Therefore, the temperature above 550°C

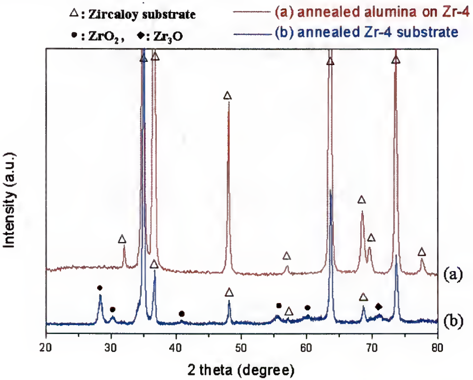

Figure 4.2. XRD spectra of (a) the amorphous alumina coated Zircaloy annealed at 500°C for 2h and (b) the uncoated Zircaloy substrate annealed at 500°C for 2h (b)

could enhance the diffusion of oxygen (as well as zirconium elements) through the amorphous alumina coating and enhance the reaction of oxygen and zirconium to make zirconium oxide such as ZrO_2 as well as Zr_3O. As discussed above, the small peaks that existed in the coated sample disappeared in the uncoated sample because the grown zirconium oxides reduced the amount of the detection of the small peaks.

AES depth profiles of as-deposited, 450°C, 500°C and 550°C annealed Al_2O_3 coatings on Zircaloy substrates were shown in Figure 4.3. AES depth profile of the 650°C annealed sample couldn't be obtained because of the surface charging. Annealing was performed in air for 2 hours. AES depth profiles of the samples annealed below 550°C showed the almost similar peaks to that of the as-deposited sample. Annealing just enhanced the interdiffusion of Al, O and Zr a littile bit. At 550°C, the amount of oxygen was increased in the interface region suggesting the initial stage of the formation of zirconium oxide as suggested in XRD patterns above. It is also observed that the concentration of oxygen in the alumina region near the interface was also increased. Both XRD and AES spectra didn't show the formation of any intermetallic compound.

AFM images of Al_2O_3 coatings on Si substrates using RF magnetron sputtering as-deposited, annealed at 500°C and annealed at 800°C, respectively, are shown in Figure 4.4. The surface morphology of the coating was smooth and uniform in the as-deposited sample and the 500°C annealed sample. However, the samples annealed at 800°C showed a rough surface, which seemed to be due to the grains of γ-alumina. As mentioned before, since the temperature of crystallization of alumina is 730°C, there could be the phase transformation of amorphous alumina into γ-alumina in the coating annealed at the temperature as high as 800°C. If then, there should be a large volume change and

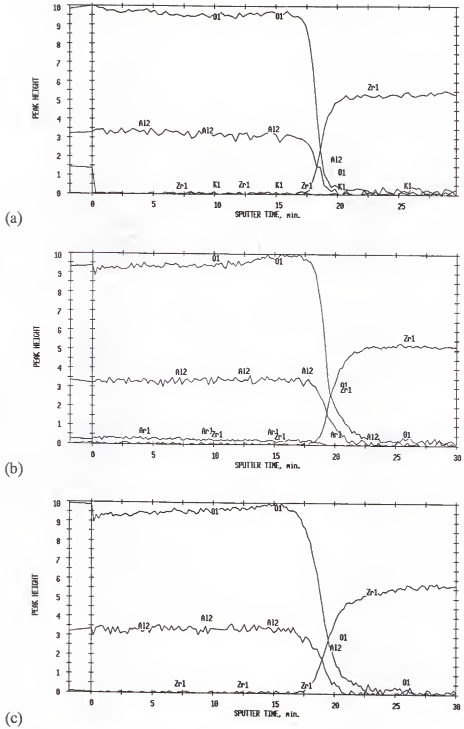

Figure 4.3. AES depth profiles of Al_2O_3 coatings on Zircaloy substrates, using RF magnetron sputtering. Annealing was performed in air for 2 h (a) As-deposited (b) 450°C annealed (c) 500°C annealed (d) 550°C annealed

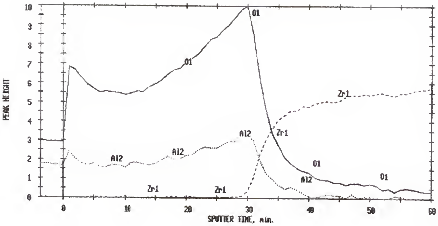

(d)

Figure 4.3. continued

consequent failure due to the difference of CTE even if the temperature was still below the temperature of the allotropic transformation of Zircaloy. Note that the scale of z-axis is expanded considerably compared with the x- and the y-axis to distinguish the difference in the roughness of the samples.

4.2.3 Mechanical Properties

Figure 4.5 shows the results of the stylus profilometer scans showing the surface profile and roughness of the Zircaloy substrate polished with different grit size or suspension particle size used as polishing media. Surface roughness of the Zircaloy substrates was so high that nanoindentation test couldn't be performed.

For the application of protective coatings to nuclear service, it is desirable to have coatings with improved strength and corrosion resistance in high-temperature water or steam. The surface of the cladding need to be hard and durable because there is a fretting due to the collision of the fragments existing in the water in the reactor and the cladding can get some scratches or scars on the surface during handling.

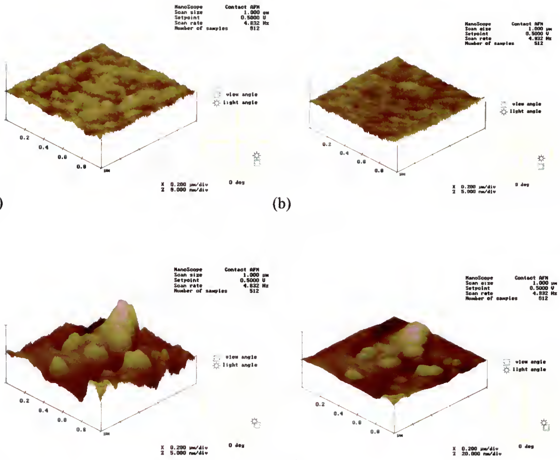

(a) (b)

(c) (c)'

(c' is different Z value of 20nm)

Figure 4.4. AFM images of (a) as-deposited, (b) 500°C annealed and (c) 800°C annealed Al_2O_3 coatings on Si substrates, using RF magnetron sputtering. Annealing was performed in air for 2 hours

Figure 4.6 shows the nano indentation load-unload curves of the sputter deposited amorphous thin films as-deposited, annealed at 500°C and annealed at 800°C for 2 hours in air, respectively. Curve shapes are almost exactly same to each other. However, the applied forces to get to the same displacement depth, which is related with modulus and hardness were different from each other. Although the difference was very small it was inversely proportional to the annealing temperature. Contact depths of the samples are as shown in the box in Figure 4.6.

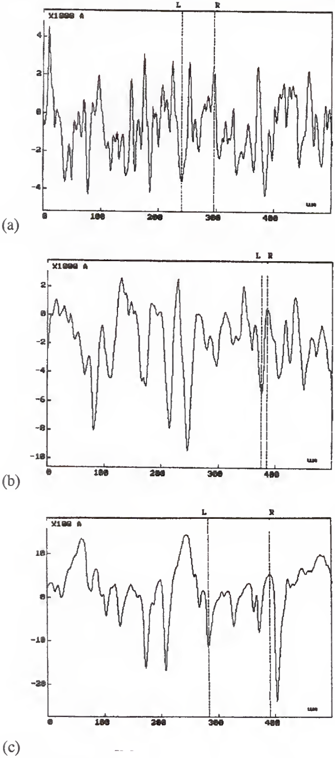

Figure 4.5. Profilometry surface scan profiles of the Zircaloy substrates polished with different grit size or suspension particle size used as polishing media; polished with (a) 600grit SiC paper, (b) 5μm alumina particles and (c) 1μm alumina particles

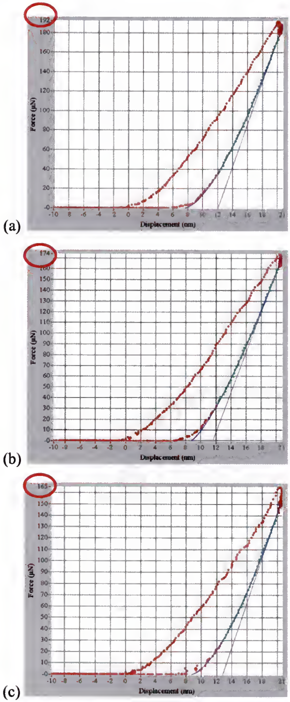

Contact Depth (nm)
500C: contact depth: 13.75 (SD:0.4416)
800C: contact depth: 13.79, (SD:0.9436)
As-depo: contact depth: 14.26, (SD:1.07)

Figure 4.6. Nano indentation load-unload curves of the sputter deposited amorphous thin films; (a) as-deposited, (b) annealed at 500°C and (c) annealed at 800°C for 2 hours in air

The stiffness of the coating is the slope at the initial point of a unload curve. It is used to calculate the hardness and modulus using nanoindentation analysis as introduced in section 3.4 in this dissertation. The results are shown in Figure 4.7 below. The

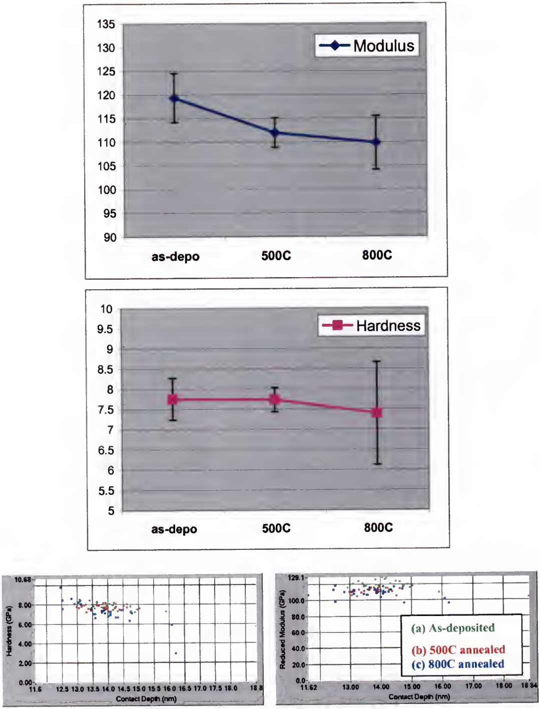

Figure 4.7. Hardness and modulus plots and graphs of the sputter deposited amorphous thin films; (a) as-deposited, (b) annealed at 500°C and (c) annealed at 800°C for 2 hours in air

hardness and modulus were the average values of the results calculated from 30 repeated indentations. The values were very similar to each other showing very little differences of average values. The values were inversely proportional to the annealing temperature. The difference may be related with the structure and consequent morphology change as shown in AFM images in Figure 4.4. The larger standard deviation in the sample annealed at 800°C was thought to be due to the non-uniform surface properties induced by the localized phase or structure change. Bunshah [103] mentioned that the hardness of a material may be influenced by the

grain size, dispersed phases, defect structure, microstructure, density, temperature, deformation rate, etc. It was reported that hardness of alumina was inversely proportional to the substrate temperature in the temperature range below 900°C [104].

4.2.3 Influence of Sputtering Gas Ratio on Stochiometry

In most cases, sputter deposition of a compound material from a compound target results in a loss of some of the more volatile material (e.g., oxygen from oxide) and this loss is often made up by deposition in an ambient containing a partial pressure of the reactive gas. This process is called “quasi-reactive sputter deposition”. In quasi-reactive sputter deposition, the partial pressure of reactive gas that is needed is less than that used for reactive sputter deposition.

Oxygen percentage in sputtering gas has been varied from 0% to 50%. Argon was used for the sputtering gas. Figure 4.8 shows the variation of aluminum and oxygen element concentration with varying ratio of oxygen reactive gas to argon sputtering gas during the sputter deposition. In our case there have been no volatilization of oxygen during the sputtering. The film deposited with no oxygen showed the exact stochiometry of alumina while the films with 25% as well as 50% oxygen showed the excess oxygen concentration in the grown films by sputtering.

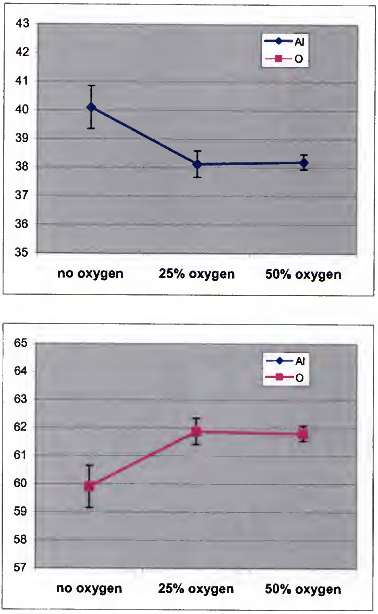

Figure 4.8. The variation of (a) aluminum and (b) oxygen concentration in the deposited films with varying ratio of oxygen reactive gas to argon sputtering gas during the sputter deposition

CHAPTER 5
CONTINUOUS COMPOSITIONAL GRADIENT COATINGS THROUGH CONTROLLED HEAT TREATMENT OF ALUMINUM FILMS ON ZIRCALOY

5.1 Introduction

Ceramic surface coatings have been used in various fields as protective coatings such as thermal barrier coatings [7-12], wear protective coatings [13-15] and corrosion protective coatings [16-22]. Only a few studies have been reported for PWR cladding protection. Thin surface coatings have been suggested as a possible means for Zircaloy cladding corrosion prevention [22-26]. Ceramic coatings are increasingly being used to protect metals in corrosive environments due to their suitable properties and to the possibility of tightly adhering them to metals. However, the coating may easily fail because of the poor bonding between the ceramic coating and the metal substrate. Their limitations are not generally due to the ceramic coating itself but rather by the interface quality such as adhesion that is reflected by the fracture resistance of the metal/ceramic interface [27-29].

It has been reported[67, 69, 70, 73-75] that functionally gradient coatings have been utilized to improve the adhesion properties by reducing the thermal expansion mismatch, and interfacial stresses between the coating and substrate. This thermal expansion mismatch and stresses are responsible for interface delamination and film spalling damage [30, 31]. Functionally gradient materials (FGMs) can be considered as a sort of composite whose composition varies with thickness according to performance requirements. Such materials have the potential for a wide range of thermal and structural applications including thermal gradient structures, wear and corrosion resistant coatings and metal/ceramic joining. The coating can be fabricated to be a composite with the local volume fraction of metal varying through the coating thickness, mimicking an inclusion/matrix type FGM or a FGM multilayer.

However, there is a problem since FGM should have the diffusion type interfaces. A problem with the diffusion type interface may be the development of voids in the interphasal material if the diffusion rates of the materials are different (Kirkendall voids). Diffusion can be accompanied by reaction to form a compound material. The interphase material formed may be brittle, have Kirkendall voids, and develop microcracks due to the stresses developed in forming the compound material – all of which reduce the fracture strength of the interface region and hence lower the film adhesion. It has been reported that physical mixing of the depositing materials by implantation of atoms into the substrate surface or surface alloying by laser to avoid the problem as described above has been used to form a pseudodiffusion type of interface under low-temperature conditions or when the materials are insoluble. However, this kind of process has the problem of high cost and is restricted to a small area on the target materials.

We introduce the advanced interlayer system for adhesion improvement, which can effectively reduced interface defects such as voids and microcracks formed due to the stress in the high temperature process by controlled heat treatment to adjust the diffusion rates of the elements in the system. It can also relax the stress created in the process. It has the advantages of the physical mixing methods by implantation or step multilayer film deposition. Our process excludes the disadvantages of those other processes such as high cost.

In this chapter, we proposed the compositional gradient coatings through controlled heat treatment as a corrosion protection system for the Zircaloy cladding in PWR's. Aluminum films were deposited on Zircaloy substrates by electron-beam evaporation and heat-treated by controlled annealing at near the melting temperature of aluminum. Two different heat treatments procedures of step-wise and isothermal annealing were employed to make the compositional gradient layers. The substrate surface aluminum film thickness, and air oxidation time and temperature were varied to optimize the film structure.

5.2 As-Deposited Aluminum Metal Coatings

The AES depth profile of a deposited aluminum film is shown in Figures 5.1. As shown in the profile, only a pure aluminum film was deposited on Zircaloy substrate without any other elements. There is some oxygen present at the interface, which could be due to oxides produced during the polishing procedure. Figure 5.2 shows an EDX spectrum obtained from the film. The presence of zirconium in the EDX spectrum is

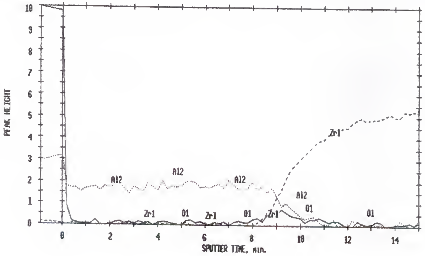

Figure 5.1. AES depth profile of an aluminum metal film with the thickness of 500nm deposited on a Zircaloy substrate by electron beam evaporation.

from substrate since the penetration depth of x-rays (1 μm) exceeds the deposited film thickness and Pd is due to Au-Pd overcoating on sample surface to minimize the electric charging in the SEM analysis.

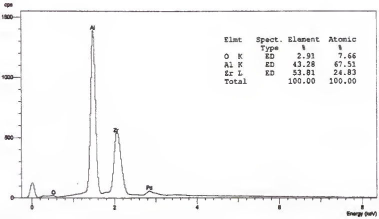

Elmt	Spect. Type	Element %	Atomic %
O K	ED	2.91	7.66
Al K	ED	43.28	67.51
Zr L	ED	53.81	24.83
Total		100.00	100.00

Figure 5.2. EDX analysis results of an aluminum metal film deposited onto a Zircaloy substrate by electron beam evaporation.

5.3 Temperature Dependence

AES depth profiles were collected for the aluminum films deposited on Zircaloy with a thickness of 30nm after oxidation by annealing for 2 hours at 400°C, 500°C and 600°C, respectively (Figure 5.3). While the aluminum oxides were formed only at the top surface of the film at 400°C, the oxygen could penetrate into the inside of the films to a degree at the temperature above 500°C. The aluminum and the zirconium inter-diffused into each other so that they formed an intermetallic region as well as the oxide region by the reaction of aluminum with oxygen in air atmosphere. The pattern of the profile shows the compositional gradient layers. However, thicker oxide regions are needed in order to obtain higher resistance [105-107]. The films annealed at 600°C showed a similar structure to the films at 500°C. Comparing with the case at 500°C, while aluminum diffused deeper, the depth of the oxygen penetration was decreased. This suggests that

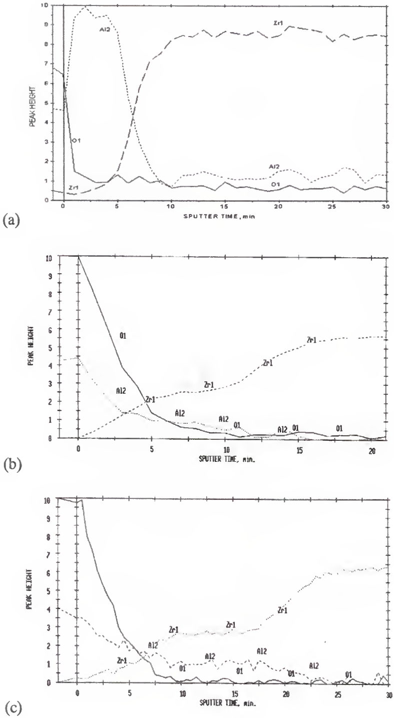

Figure 5.3. The AES depth profiles of the oxidized aluminum films on Zircaloy with a thickness of 300 nm after annealing for 2 hours at various temperature of (a) 400°C, (b) 500°C and (c) 600°C, respectively.

there was a change in diffusion rates of the elements at the different temperatures. It should be noted that since the cladding will be maintained at less than 600°C related to the PWR operation temperature and that structure change, as mentioned in chapter 2 [101, 102], and the substrate structure will be changed above the temperature of 600°C when it is exposed to the high temperature condition for a long period as reported [108, 109]. The difference in sputter times on the x-axis is due to the change of the raster size of the AES sputtering to decrease the analyzing time because oxides require more sputtering time. The highest point in peak height on the y-axis was made to automatically fit to the top of the graph by the software.

5.4 Annealing Time Dependence

Figure 5.4 shows the AES depth profiles of the oxidized aluminum films on Zircaloy after annealing at 500°C for 1 hour, 2 hours and 3 hours, respectively. In the coating annealed for 1 hour (a), the oxygen could penetrated into the aluminum film half way down to the interface. A small amount of both the aluminum and the oxygen went through into the substrate. The interface was still distinguishable on the profile. With increased annealing time of 2 hours, the oxygen penetrated through the aluminum film and reached the substrate (b). The aluminum and the zirconium also inter-diffused into each other. A definable interface was not observed. A compositional gradient structure was eventually formed. However, graded intermetallic regions expected to play a role as a bonding layer between oxide regions and substrates scarcely exist. It was shown that the more annealing time destroyed the linear gradient structure indicating too high of an oxygen content in the middle of the film in Figure 5.4 (c). The highest point in peak

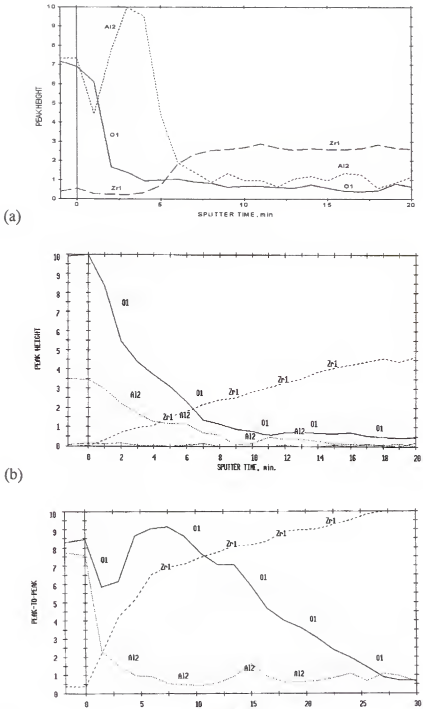

Figure 5.4. The AES depth profiles of the oxidized aluminum films on Zircaloy with a thicknesses of 100 nm after annealing at 500°C for various times of (a) 1 hour, (b) 2 hours and (c) 3 hours, respectively.

height on the y-axis was automatically forced to fit to the top of the graph by the software.

5.5 Thickness Dependence

The non-linear structure in Figure 5.4(c) may be due to the relatively low film thickness. Figure 5.5 shows the AES depth profile of the oxidized aluminum films on Zircaloy with increased thickness of 300 nm after annealing at 500°C for 3 hours. Less oxygen diffused into the inside of the film and excess diffusion of zirconium was decreased. Therefore, the annealing time could be optimized to 2 hours as shown in Figure5.3. However, intermetallic regions as a bond layer were not observed in this case.

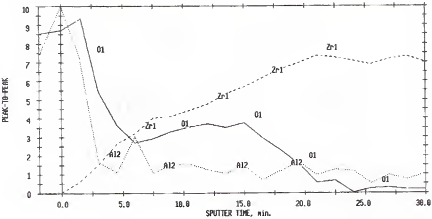

Figure 5.5. The AES depth profiles of the oxidized aluminum films on Zircaloy with a thicknesses of 300 nm after annealing at 500°C for 3 hours.

Delamination and cracks are usually created by residual stresses between films or tin the films, which could be due to thermal expansion. Generally, it is believed that adhesion increases with increasing thickness of coatings [110, 111]. However, it is believed that the increase in adhesion with film thickness does not represent an increase in adhesion of the coating but it is a feature of a buckling failure mode [112]. Adhesion of coatings tested by the scraping method was found to decrease with increasing film

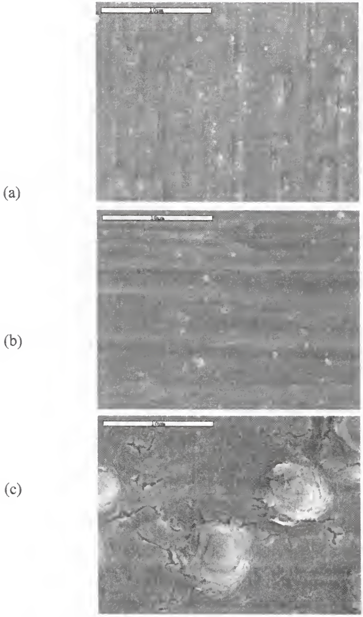

Figure5.6. The SEM pictures of the oxidized aluminum films whose thickness of (a) 100 nm, (b) 300 nm and (c) 5000 nm on Zircaloy after annealing at 500°C for 2 hours

thickness in contrast to generally accepted theories [113]. In the SEM pictures of the oxidized aluminum films whose thickness of 100 nm on Zircaloy after annealing at 500C for 2 hours (Figure5.6 (a)), no apparent delamination were found and just a few tiny cracks were observed. The films were smooth and uniform. A sample with a thickness of

300 nm shown in Figure5.6 (b) was also observed not to have any significant failure. However, as the thickness was increased to 500 nm with the same condition of annealing, many island-like buckled areas with significant cracks around the buckled areas were observed as shown in Figure5.6 (c). These island-like buckled area looked like partially delaminated area and were combined with cracks that were around the area. Therefore, the film thickness was optimized to 300 nm in this work.

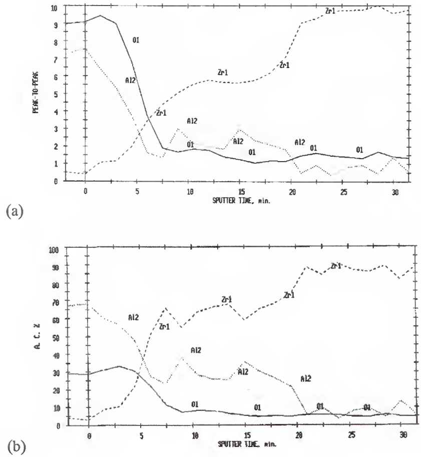

Figure 5.7. AES depth profiles of a 300 nm aluminum films oxidized at 650°C for 30min followed by at 500°C for 2hrs: peak heights and atomic concentrations are marked on the y-axis in (a) and (b), respectively

5.6 Controlled Two-Step Heat Treatment

Figure 5.7 shows the AES depth profiles of the 300 nm aluminum films on Zircaloy oxidized at 650°C for 30 minutes followed by a 500°C treatment for 2 hours in air. It is probable that aluminum diffused into the sample to a great depth using the two-step heating process because the annealing temperature was near the melting temperature of aluminum. The oxygen diffusion into the sample is greater for the two-step heat treatment than isothermal heating shown in Figure5.3 (b). These depth profiles demonstrate that the compositional gradient film structure was achieved with proper intermetallic regions and oxide regions using the controlled heat treatment method. The compositionally quantified profile calculated by the method introduced in section 3.4 is shown in Figure 5.7 (b). Aluminum and oxygen amounts in the films are clearly shown in this figure.

The SEM micrograph for a 300 nm aluminum film oxidized by isothermal annealing and by step annealing are shown in Figure5.8 (a) and Figure5.8 (b), respectively. Total annealing time for these two samples were the same because the step annealing required heating and cooling stages between the two different annealing

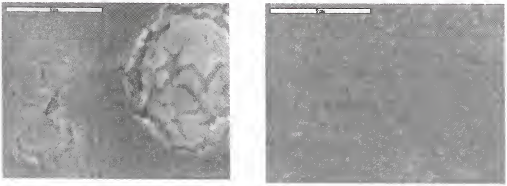

Figure 5.8. SEM micrograph of a 300 nm aluminum film deposited on Zircaloy after (a) oxidizing at 500°C for 3hrs and (b) oxidizing at 650°C for 30min followed by at 500°C for 2hrs

temperatures. *While the buckled regions with some cracks were broken out on the sample surfaces in the isothermal annealing, the surface had no significant failure like cracks or delamination in the two-step annealed sample.*

5.7 Phase Identification

The AES results in Figure 5.3 and 5.7 suggested the possibility of the samples having multi-phases in the coatings after heat treatment. The glancing angle x-ray diffraction (GAXRD) results revealed that there are multiple crystalline phases in the oxidized coatings. Figure 5.9 shows the GA XRD results for a 300 nm coating oxidized with two different heating schedules, along with an unheated sample. The diffraction pattern of the film without heat treatment (c) shows only zirconium and aluminum metal. After 30min at 650°C annealing (b) i.e. the first stage of step-wise annealing, various intermetallic and oxide phases appeared, including Al_3Zr, ZrO_2 and Al_2O_3. Some peaks could not be identified. With a further annealing at 500C for 2hours (a) as the completion of the controlled heat treatment, additional Al_2Zr_3 phase was formed and ZrO_2 phase disappeared. It can be inferred that Zr diffused further for the longer exposure time to form a Zr-rich phases rather than Al-rich phases which were formed with a short annealing time at the higher temperature (shown in (b)). These Al-Zr intermetallic compounds were not found in the alumina coating deposited on Zircaloy by sputtering, which was introduced in chapter 4. In sputter deposited alumina film, oxygen could penetrate the amorphous film to the substrate and react with zirconium and form the zirconium oxides. In this case, oxygen from ambient reacted with aluminum metal before it might get to the substrate, and formed a kind of aluminum oxide while Al and Zr reacted each other to form intermetallic compounds.

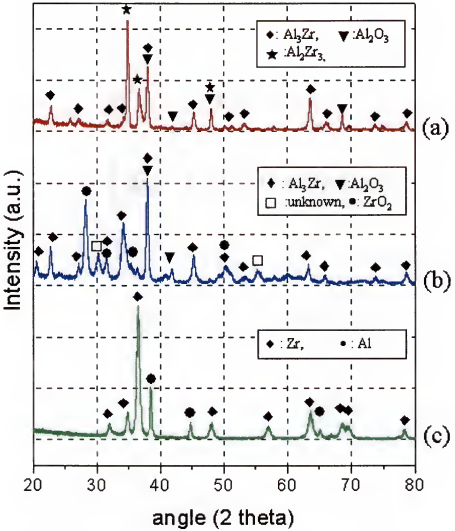

Figure5.9. GAXRD (glancing angle incident x-ray diffraction) spectra of a 300 nm aluminum film deposited on Zircaloy annealed (a) at 650°C for 30min followed by at 500°C for 2hrs, (b) at 650°C for 30min and (c) as-deposited (no annealing)

The step-wise annealing had an effect on not only the compositional gradient distribution in the depth profile, but also the formation of the intermetallic phases in the films.

It was necessary to clarify the existence of the multi phases since the several peaks in the XRD diffraction patterns of the existing phases overlapped and consequently the identification couldn't be accurate. That verification of multi phases could be completed by the AES multiplex spectra of aluminum and oxygen through the film as shown in Figure 5.10. A peak shift took place in the AES spectra, which reflects a change of the bond structure. Different kinetic energies of the auger electrons showed the different

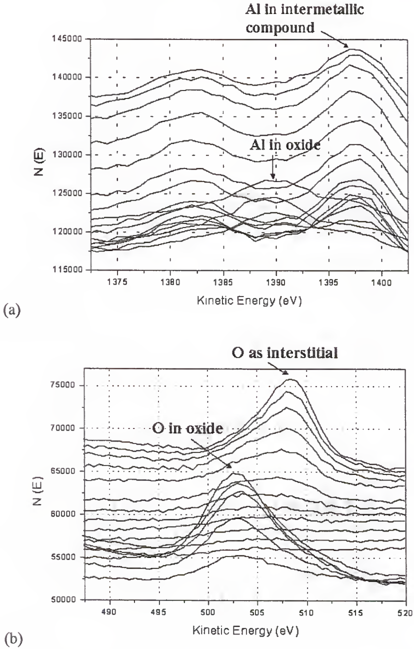

Figure 5.10. AES multiplex spectra in correspondence with depth profiles for (a) Al and (b) O of the 300 nm aluminum films oxidized at 650°C for 30 minutes followed by at 500°C for 2 hours. (in Figure5.7)

phases suggesting the presence of the oxides and the intermetallic phases as marked in the figures.

5.8 Cross-sectional TEM and in-situ EDS

Cross-sectional TEM pictures of the 300 nm aluminum films oxidized at 650C for 30 minutes followed by at 500C for 2 hours are shown in Figure 5.11. The pictures showed the intermetallic phases formed from aluminum metal film by the interfacial reaction through the heat treatment as verified in the section 5.7. These TEM pictures visually confirmed the formation of intermetallic compound layers with a compositional gradient. The phase boundaries were very dense and there were no crack or defects in the boundaries. EDS analyses were performed for five different locations along with the thickness. The top layer had the columnar grain structure with the composition similar to alumina, which has excess oxygen and a little zirconium diffused from the substrate. The second layer from the top was the Al_3Zr intermetallic layer with the polycrystalline structure containing relatively large grains. Although the amount of oxygen dropped abruptly compared with the top layer, it was still around 10% in the EDS results suggesting that oxygen with its small atomic size, could penetrate deeply after the formation of the thin alumina layer on the top surface. The oxygen concentration decreased at the position near the third layer making a compositional gradient of oxygen. The next layer with the increased amount of zirconium consisted of Al_2Zr_3 that was relatively thinner than the Al_3Zr layer. The oxygen was just below 5% that is in the range of error in EDS indicating that there was scarcely oxygen in the film in that area. The interface was continuous with the upper layer and still completely dense without any crack or delamination. Afterward, the concentration of zirconium gradually increased and that of aluminum decreased when eventually the substrate was reached without any apparent interface. Copper peaks in the EDS spectrum came from a copper grid containing the specimen.

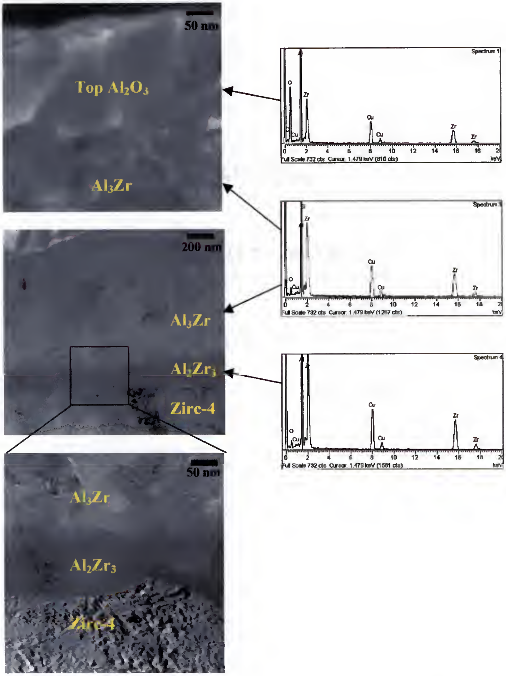

Figure 5.11. Cross-sectional TEM pictures of the 300 nm aluminum films oxidized at 650C for 30 minutes followed by at 500C for 2 hours

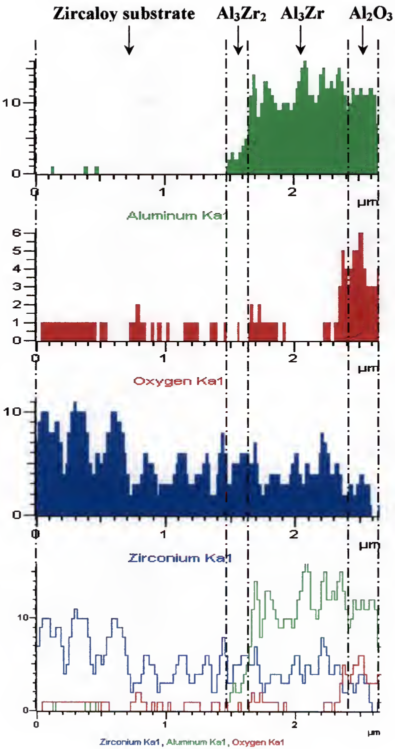

Figure 5.12. EDS line scan spectra of the $Al_2O_3/Al_3Zr/Al_2Zr_3$/Zircaloy structure shown in the TEM image (Figure5.11)

This structure was confirmed by the in-situ EDS line scan spectra as shown in Figure 5.12. Each spectrum showed the compositional gradient and the distribution along the depth of the coating system. Zirconium was found at the nearly top of the coating and oxygen at the deep inside of the substrate as an impurity. The compositional distribution was more distinct here than in the AES depth profile in Figure 5.7. The compositional structure of $Al_2O_3/Al_3Zr/Al_2Zr_3$/Zircaloy was marked on the basis of the spectrum intensities and distributions.

Figure 5.13 is the plots of the EDS quantification data at the specific four spots with the thickness in the coating system. Because the graph indicates not the absolute amounts of the elements but the percentage of the element concentration, the graph didn't show the graded shape. However, the relative amount of each element nearly matched with the stochiometry of the phases suggested in the prior discussion. The stochiometric distribution of $Al_2O_3/Al_3Zr/Al_2Zr_3$/Zircaloy structure was shown clearly quantified.

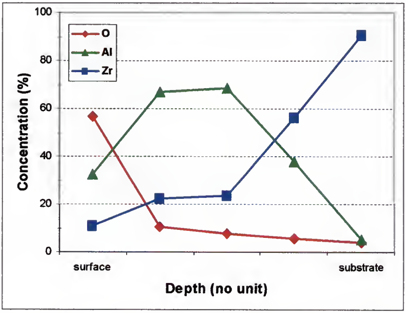

Figure 5.13. The plots with the thickness of EDS results of the 300 nm aluminum films oxidized at 650C for 30 minutes followed by at 500C for 2 hours

5.9 Atomistic and Thermodynamic Considerations

Hexagonal α-Al_2O_3 is the thermodynamically stable form of Al_2O_3 at all temperatures. However, α-Al_2O_3 has experimentally formed only at elevated substrate or annealing temperatures (~1100°C). Therefore, these observations suggest that kinetic barriers, possibly associated with covalent bond angle requirements, prohibit the formation of the equilibrium α-structure by the normally large surface diffusion processes. Therefore, it was inferred that the metastable alumina such as γ- or κ- Al_2O_3 was formed easily rather than α-structure.

Thermodynamic data in Table 5.1 shows the negative values of the free energy of formation of some polymorphic aluminas, suggesting that the reactions between the oxygen and aluminum described above would be able to take place spontaneously.

Table.5.1 Thermodynamic data for alumina top layer [114]

$2\,Al + 3/2\,O_2 \rightarrow Al_2O_3$

Gibbs free energy of formation at 900 °K (628°C) (unit: kJ mol^{-1})		
α- Al_2O_3	:	ΔG_f° = - 1393.91
δ- Al_2O_3	:	ΔG_f° = - 1385.58
γ- Al_2O_3	:	ΔG_f° = - 1378.13
κ- Al_2O_3	:	ΔG_f° = - 1383.72

Since the annealing process was performed at the high temperature of 500°C to 650°C, diffusion phenomena should be take place in the system. Al, Zr and O were moving species and would be assumed to follow the equation below.

$$D = D_o \exp(-\frac{Q_d}{RT}) \tag{5.1}$$

The atomic sizes of the moving species are as shown in the Table.5.2 below. Since the atomic sizes of Al and Zr are similar each other, Zr diffusion mode in Al should be substitutional mode. Also, since atomic size of oxygen is much smaller than Al, oxygen diffusion mode should be interstitial diffusion, which indicates that the activation energy for Zr diffusion should be larger than that for O diffusion. Consequently, the diffusion coefficient, in other words, diffusion rate of O is higher than that of Zr (approximately 10^5 times). Conclusively, the controlled step-wise heat treatment could maximize the interdiffusion rate of Al and Zr with the annealing near the melting temperature of Al. Al could react with Zr to form Al-Zr intermetallic layers, before O reached the substrate and reacted with Zr to form ZrO_2.

Table 5.2 Atomic radius and structure of moving species [114]

Element	Atomic radius	Atomic structure
Al	1.43 A	FCC
Zr	1.60A	hexagonal
O	0.6A	

The Al-Zr system has one of the more complicated binary transition metal phase diagrams. Ten intermediate phases belonging to four different crystal systems were reported as shown in Figure 5.14.

Laik reported[115] that the intermetallic phase $ZrAl_3$ forms in the diffusion zone in all the diffusion couples in planar morphology. The formation of $ZrAl_3$ as the first phase was rationalized on the basis of the modified effective heat of formation model. The appearance of Zr_2Al_3 in preference to $ZrAl_2$ at higher temperatures is attributed to the higher driving force for its formation at the Zr/$ZrAl_3$ interface. Therefore, the thicker Al_3Zr layer in our system should have formed at the first stage and Al_3Zr_2 might be formed in preference to Al_2Zr. Afterward, the thin Al_2Zr_3 layer could be formed through the further proceeded diffusion process. In addition, as reported by Deqing[116], the reduction of zirconium oxide can be driven thermodynamically by the dissolution of Zr in aluminum. Because the solubility of Zr in aluminum is quite small the formation of $ZrAl_3$ is favored after relatively small Zr dissolutions. This suggests that the small amount of ZiO_2 phase formed at the initial stage in the heat treatment could be dissolved when Al_3Zr phase began to form and absorb Zr.

Yanagisawa[117] has reported that the interposition of an intermediate Al_3Zr layer could successfully suppress the possible spontaneous reactions between the Al and Zr layers due to nearly-minimum free energy states. Because a stable Al_3Zr intermetallic compound formed during the heat treatment above 400°C in the thermal equilibrium state, no more solid-phase reaction take place in the system. This report suggests that Al_3Zr layer could function to prevent the formation of zirconium oxide in our system.

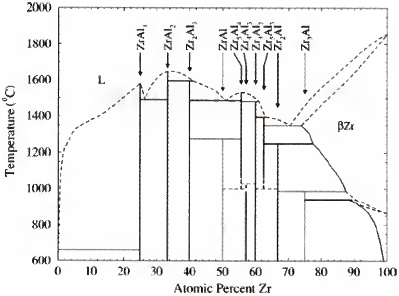

Figure 5.14. Schematic phase diagram for Al-Zr [33]

5.10 Summary

The aluminum based compositional gradient structures were fabricated to develop ceramic coating corrosion protection systems for Zircaloy fuel rod cladding in pressurized water reactor (PWR) nuclear reactors. Aluminum films were deposited on Zircaloy substrates by the electron-beam evaporation and surface-alloyed by the controlled oxidation at near the melting temperature of the aluminum. Two different oxidation procedures were employed to make compositional gradient compound layers. The aluminum film thickness, air oxidation time and temperature were varied. The film with the thickness of 300nm with isothermal annealing at 500°C for 2 hours in air showed that the gradient compositions of Al, Zr, and O vary through the coatings thickness by AES depth profiles. They didn't show cracks or delamination in the FE SEM images. Additional annealing at 650°C for 30 min prior to isothermal annealing, described above, increased both the oxide region acting as a corrosion resistant layer and the intermetallic region acting as an interlayer for adhesion improvement. Glancing angle x-ray diffraction (GAXRD) analysis showed that a variety of intermetallic and oxide phases (such as Al_3Zr, Al_2Zr_3, Al_2O_3, ZrO_2 and Zr_3O) were formed in the coatings during processing. AES multiplex spectra also showed the peak shifts in Al and O verifying the existence of multi-phases. HRTEM images and in-situ EDS data clearly showed the formation of the compositional gradient intermetallic layer structure with quite accurate stochiometry. The mechanism of the formation of the intermetallic compound layers was considered atomistically and thermodynamically. The appearance of Zr_2Al_3 in preference at higher temperatures is attributed to the higher driving force for its formation. It is suggested that Al_3Zr can function to prevent the formation of zirconium oxide.

CHAPTER 6
EFFECT OF THE COMPOSITIONAL GRADIENT LAYER AS AN INTERLAYER BETWEEN AMORPHOUS ALUMINA THIN FILM AND ZIRCALOY SUBSTRATE

6.1 Introduction

Amorphous alumina coatings were introduced for the oxidation protection system for Zircaloy cladding used in nuclear reactor in chapter 4. In a previous chapter, the compositional gradient coatings for oxidation protection were also suggested with their components of oxide and intermetallic compound layers.

However, these two ways for the oxidation protection system can have some problems when they are used individually. The single coating of amorphous alumina can still confront the fundamental issue of adhesion due to the heterogeneous feature of the ceramic/metal interface although the selection of material could reduce the problem to a degree. The compositional gradient layer (CGL) process can have a problem when the system is used for long term period since the coating is relatively thinner than the coating that is being used for this purpose generally. In addition, as mentioned in chapter 4, the system requires the good mechanical properties such as hardness.

Therefore, we propose the structure of a-Al_2O_3/CGL/Zircaloy that is the combination of the two coating systems we discussed above earlier. The amorphous alumina thin films discussed in chapter 4 were deposited on the compositional gradient layers (CGLs) handled in chapter 5. In this chapter, the effect of compositional gradient layer on the properties of the oxidation protection system will be discussed.

6.2 Proposed Model for Oxidation Protection System

The schematics of the model based on Al-Zr phase diagram in equilibrium and the model completed by the experimental using the controlled heat treatment are described in Figure 6.1. Several intermetallic compound layers with the formula varying along with the gradient was proposed initially based on equilibrium phase diagram. The solid solutions having the graded concentration in the inter region between the layers surrounding them were expected to be formed preventing the interface failure. However, after the controlled heat treatment explained in the prior chapters, Al_2O_3/Al_3Zr/Al_2Zr_3 /Zircaloy structure without any solid solution area as well as any interphase failure was created thermodynamically, which was interpreted in the previous chapter. The addition of top amorphous alumina deposition made the double alumina structure of amorphous alumina on crystalline columnar γ-alumina. The top amorphous alumina layer and the compositional gradient intermetallic layer can play a role as the protective system. However the columnar crystalline alumina layer between those two layers is thought to allow the migration of oxygen along the void between each column. In other words, it doesn't provide the additional oxidation resistance. Instead, the adhesion between the two layers of the upper alumina layer and bottom Al_3Zr layer of it should be affected by this alumina columnar layer. This adhesion property will be discussed in the section 6.4 later.

6.3 Prevention of the Formation of Zirconium Oxide

XRD spectra of the aluminum films oxidized at 650C for 30 minutes followed by at 500C for 2 hours (Figure5.9. (b)) and that of the uncoated Zircaloy substrate with the same heat treatment are shown in Figure 6.2. The XRD pattern of Zircaloy annealed at 650C for 30 minutes followed by at 500C for 2 hours shows that zirconium had reacted with oxygen in air atmosphere and formed the zirconium oxides such as ZrO_2 and Zr_3O.

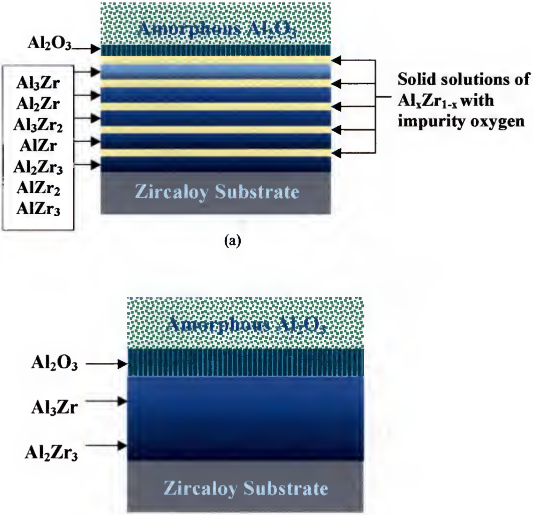

(a)

(b)

Figure 6.1. The schematics of (a) the model based on Al-Zr phase diagram in equilibrium and (b) the model completed by the experimental using the controlled heat treatment.

However, the XRD spectrum of aluminum film on Zircaloy with the same heat treatment showed no zirconium oxide phase but the intermetallic compound phases of Al_3Zr and Al_2Zr_3. This XRD results suggested that amorphous alumina coating played a role as a protector to avoid the penetration of oxygen and the intermetallic layers of Al_3Zr and Al_2Zr_3 also acted as an oxidation protection system. Therefore, the compositional gradient layer with intermetallic layers that was introduced to improve the adhesion property can also function as another barrier against the oxygen penetration.

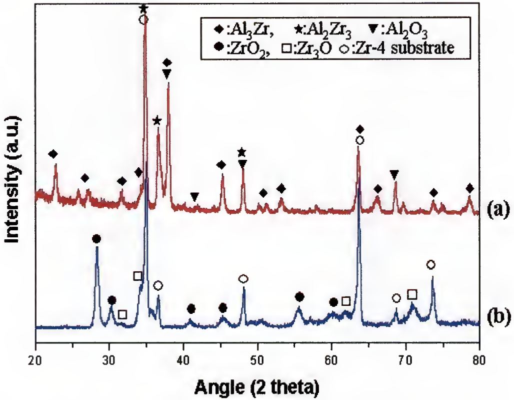

Figure 6.2. XRD spectra of (a) the aluminum film oxidized at 650C for 30 minutes followed by at 500C for 2 hours (Figure5.9. (b)) and (b) that of the uncoated Zircaloy substrate step-annealed

6.4 Improvement of Adhesion

As mentioned in the previous chapter, a problem with the diffusion type interface may have Kirkendall voids developed in the interfacial (interphase) material if the diffusion rates of the materials are different. Microcracks may be created due to the stresses developed in forming the compound material. These voids and microcracks by the applied stress reduce the fracture strength of the interface region and hence lower the film adhesion. The advanced interlayer system proposed in this research for adhesion

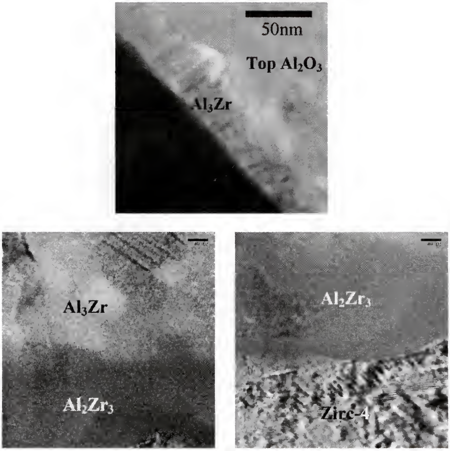

Figure 6.3. TEM images of amorphous alumina thin film on the aluminum film oxidized at 650C for 30 minutes followed by at 500C for 2 hours. Note the continuous and integrated interfaces between each layer.

improvement, which has the minimized interface defects such as voids and microcracks by annealing the stress using the controlled heat treatment, can be created by changing diffusion rates of the component materials as described in the previous chapter.

Amorphous alumina films discussed in chapter 4 were deposited on the structure of compositional gradient layer on Zircaloy introduced in chapter 5. The TEM images of amorphous alumina thin film on the aluminum film oxidized at 650°C for 30 minutes followed by at 500°C for 2 hours is shown in Figure 6.3. The image showed that there were no interphase defects and the phase boundaries were well integrated to exhibit the good adhesion property.

Scratch testing is a good method for estimating adhesion. The scratch test method consists of the generation of scratches with a spherical stylus (generally Rockwell C diamond, tip radius 2μm), which is drawn at a constant speed across the coating substrate system to be tested, under either constant or progressive loading at a fixed rate. For progressive loading, the critical load (L_c) is defined as the smallest load at which a recognizable failure occurs; for the constant loading mode, the critical load corresponds to the load at which a regular occurrence of such failure along the track is observed.

The scratch test is basically a comparison test. The critical loads depend, of course, on the mechanical strength (adhesion, cohesion) of a coating to substrate but also on several other parameters: some of them are directly related to the test itself, while others are related to the coating-substrate system. The test specific parameters include loading rate, scratching speed, indenter tip radius, and indenter material (and also tip wear). The coating-substrate specific parameters include substrate hardness and roughness, coating thickness and roughness, friction coefficient between coating and indenter, internal stresses in the coating.

Figure6.4 is the optical microscope images after scratch tests for amorphous alumina film on Zircaloy and amorphous alumina film Zircaloy with the compositional gradient interlayer (CGL). In the images, '1st chip' is when the first damage on the surface was observed, 'delamination' is when the substrate was exposed, 'continuous delamination' is that it is from that point on, and 'intermittent delamination' is that it is not continuous. Every failure is either more related to the delamination part or to more cohesive failure.

The following tables show, for each sample, the critical force L_C at which damage

Without CGL (500x)
1st Chip

With CGL (500x)
1st Chip

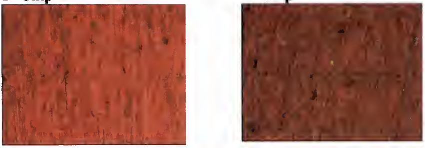

Delamination

Delamination

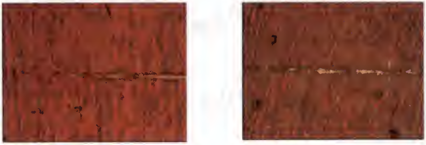

Continuous Delamination

Intermittent Delamination

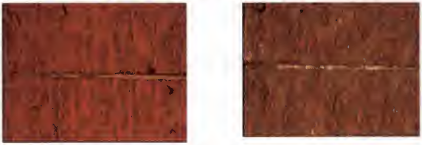

Figure6.4. The optical microscope images after scratch tests for (a) amorphous alumina film on Zircaloy and (b) amorphous alumina film Zircaloy with the compositional gradient interlayer

of the coating occurs. Delamination value is much more than 1st chip value in coating with CGL rather than in the coating with CGL. That is because 1st chipping will be more influence by local variation since a small defect on your coating might trigger it, while delamination is the general strength/adhesion of the coating.

'Delamination' in the table is the first time when the substrate was exposed. It is normally influenced by local variation. A rougher sample would probably fail at first but

Table 6.1. Critical forces for the delaminations of the amorphous alumina films without and with the compositional gradient interlayer

Without Compositional Gradient Layer (RS25-2)				
	1st Chip [mN]	**Delamination [mN]**	**Continuous Delamination [mN]**	**Intermittent Delamination [mN]**
1	41.71	61.95	63.77	-
2	48.86	65.46	69.25	-
3	43.03	63.29	63.99	-
Average	**44.53**	**63.57**	**65.67**	-
Std dev	**3.11**	**1.45**	**2.53**	-
With Compositional Gradient Layer (A042-5)				
	1st Chip [mN]	**Delamination [mN]**	**Continuous Delamination [mN]**	**Intermittent Delamination [mN]**
1	45.18	146.89	-	237.25
2	80.71	185.31	-	259.25
3	72.20	203.12	-	266.62
Average	**66.03**	**178.44**	-	**254.37**
Std dev	**15.15**	**23.46**	-	**12.48**

it could take more time for the complete delamination. Based on this and the chipping information the coating with CGL might be rougher. This would also explain the intermittent delamination of the coating with CGL. The improved adhesion can delay the complete delamination so that results in the intermittent delamination pattern. The fact that the interlayer could make the surface of the total system rougher can also be the reason why the standard deviation is much bigger in the coating with CGL.

Figure 6.5 is the comparison graphs of the critical forces (L_c) for the delaminations of the amorphous alumina films without and with the compositional gradient interlayer. The L_c of the coatings with CGL showed the greater value in the 1st chip, delamination and especially much greater in continuous/intermittent delamination.

Conclusively, the results suggested that the amorphous alumina film with the compositional gradient interlayer (CGL) had a better adhesion than the film without CGL.

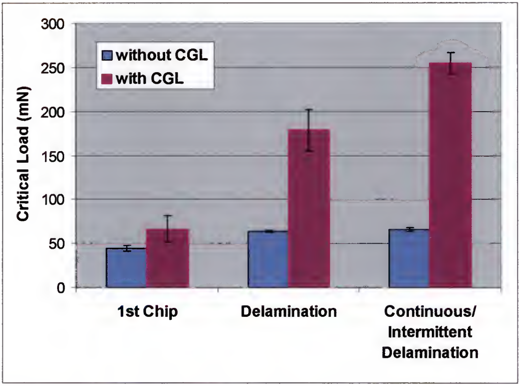

Figure 6.5. The Comparison graph of the critical forces for the delaminations of the amorphous alumina films with and without the compositional gradient interlayer

CHAPTER 7
BEHAVIOR OF SPUTTER-DEPOSITED AMORPHOUS ALUMINA THIN FILMS IN SUBCRITICAL HYDROTHERMAL CONDITIONS

7.1 Introduction

During the last two decades, sub-critical aqueous solution as well as supercritical water have been found to be a promising medium for different processes like chemical reactions[118], salt separation processes [119], extractions[120], ceramic processing[121], analytical applications, the oxidation of organic wastes (supercritical water oxidation; SCWO)[122] and nuclear reactor applications[123]. In parallel with the increasing number of applications, the need for reactor materials that can withstand the harsh conditions has increased. Oxidation of the cladding in the high temperature, high pressure aqueous environment (250~350°C, 15~20 MPa) results in the continuous formation of a zirconium oxide layer that eventually begins to spall, degrading the clad integrity, which leading to economic and environmental loss.

Alumina has many promising properties as a candidate for the cladding protection. It has a low coefficient of thermal expansion (CTE) mismatch (7.83×10^{-6}/°C) that is similar to that of Zircaloy (7.09×10^{-6}/°C) at the operating temperature range. Its good thermal conductivity has little effect upon heat transport. The neutron cross-section of alumina is low enough to not interfere the fission phenomena. Especially, there are some reports that pure alumina has very good hydrothermal durability in subcritical condition. [61]. In this chapter, the behavior of amorphous alumina thin films in subcritical water will be discussed. We believe that this is the first report about the stability of amorphous alumina, especially alumina films in subcritical water conditions.

7.2 The Behavior of Amorphous Alumina Thin Films in Subcritical Water

The surface image of as-deposited coatings by sputtering was shown in Figure 7.1(a). The SEM pictures showed the uniform and smooth surfaces. As shown in AES depth profile (Figure 7.1(b)), the as-deposited coating has abrupt interface and aluminum and oxygen elements have uniform distribution through the thickness.

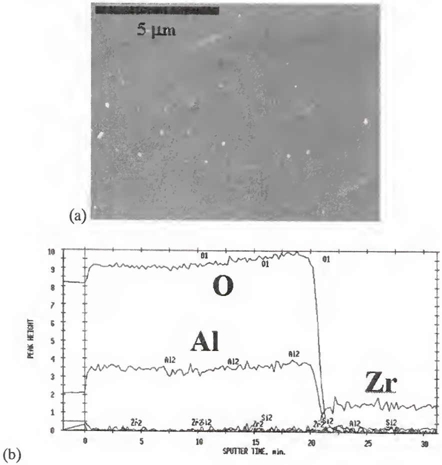

Figure 7.1. SEM image (a) and AES depth profile (b) of as-deposited alumina coatings on Zircaloy

After autoclave exposure to near-supercritical water of 20.1 MPa at 343°C for 24 hours, hydrothermally grown crystallites layers with various well-faceted shapes were observed as shown in the SEM micrograph in Figure 7.2 (a).

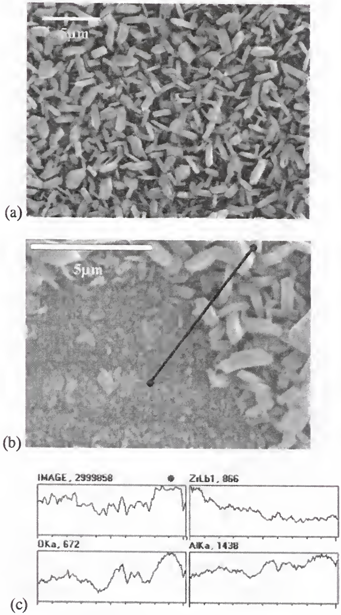

Figure 7.2. Hydrothermally grown crystallites after autoclave exposure to subcritical aqueous condition: outer layer (a), inner layer (b) and EDX line scan profile (c).

An EDX line scan result (Figure 7.2.(c)) that profiles of aluminum and oxygen are along with the image profile indicates that the compositions of outer layer and inner layer were similar to each other. The higher concentration of zirconium in the inner layer region is due to the substrate because of the lower thickness of the region. This structure of double layers is similar to the structure reported for stainless steel oxidation[124].

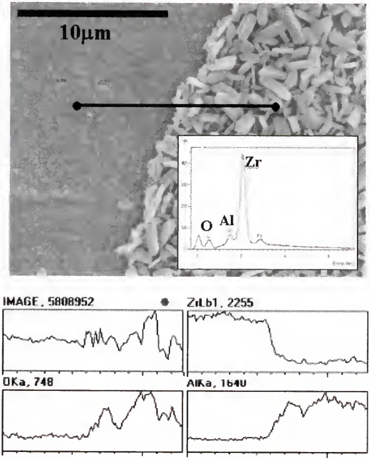

Figure 7.3. EDX spectrum and line-scan profiles of bottom layer through top layer of sputter-deposited alumina film after autoclave test.

After the autoclave test, we could also observe the small peeled off areas around the edge of the samples. Figure 7.3 is the EDX line-scan from the outer layer through the peeled-off region. In the peeled-off region, little amounts of aluminum was observed while large amount of zirconium were observed. Some oxygen was also detected as shown in EDX spectrum. Therefore, zirconium surface oxides seemed to be formed on the Zircaloy substrates.

The phases were identified by x-ray diffraction before and after autoclave test as appeared in Figure 7.4. The as-deposited alumina sample showed almost the same peak patterns as that of the Zircaloy substrates. These results indicated that alumina coatings by sputtering were amorphous as already known. However, the spectrum after autoclave exposure to subcritical water showed several extra peaks. They are identified as gamma-aluminum hydroxide called boehmite.

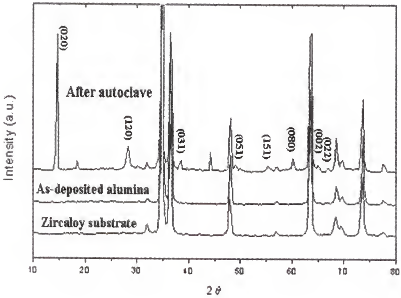

Figure 7.4. XRD spectra of sputter-deposited alumina coating after autoclave test compared with as-deposited alumina film and Zircaloy substrate. Boehmite peaks appeared after autoclave exposure.

This aluminum hydroxide formation was confirmed by XPS analysis (Figure 7.5). XPS survey spectra before and after autoclave test shows the increase of oxygen to aluminum ratio inferring phase change from aluminum oxide (Al_2O_3) to aluminum hydroxide (AlOOH). Furthermore, the peak shift of Al 2p was seen in XPS multiplex spectra. The binding energy (75.4eV) of Al 2p electron was changed to 77.3eV showing the change of surrounded elements. This result proves the phase change from alumina to aluminum hydroxide, as the peak shift is appeared as in database.

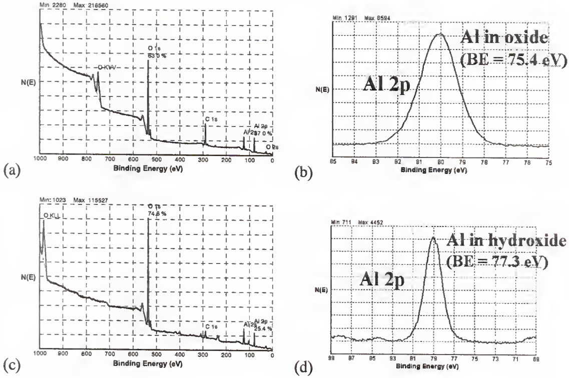

Figure 7.5. XPS survey spectra and multiplex peaks of sputter-deposited alumina coating before (a and b) and after (c and d) autoclave exposure, respectively.

There have been some reports about morphology of aluminum hydroxide formed in subcritical condition, which discussed aluminum hydroxide syntheses (Figure 7.6.) [125]. The morphology changes with temperature and pressure (especially, around the critical point). This is most likely due to the change of properties of water during the cooling process after the autoclave test, especially the dielectric constant and ion product of water affecting the solubility (i.e. degree of dissociation). The solubility of AlOOH in near-critical condition was over 10^4 times greater than that in room temperature (Figure7.7.) [126]. The particle morphology can be related to the chemical species in solution. The distribution of chemical species for the AlOOH system (Al^{3+}, $Al(OH)^{2+}$, $Al(OH)_2^+$, $Al(OH)_3$, $Al(OH)_4^-$) in subcritical and supercritical water was calculated in the report and the mechanism was proposed. Particle morphology seems to be determined by selective

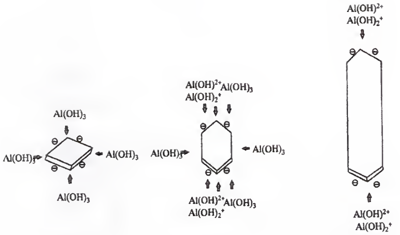

rhombic hexagonal sword-like

Figure 7.6. Morphology change of AlOOH particles with variation of chemical species distribution [125]

adsorption of positively charged species, $Al(OH)_2^+$, on the negatively charged surface of the AlOOH. The various kinds of aluminum hydroxide morphology were observed such as rhombic, hexagonal and sword-like shape (Figure 7.6.) [125]. The TEM image in Figure 7.8 confirmed that the shape of individual crystallite was exactly the same as reported. Therefore, we concluded that pure alumina amorphous coatings were transformed to aluminum hydroxide, boehmite while pure alumina bulk ceramics were stable in subcritical water as reported [61]. Thermodynamically, alumina should be stable in the water condition and cannot be transformed to hydroxide directly. The Gibb's free energy of the formation of AlOOH from Al_2O_3 in water was calculated by FactSage^{TM} and the ΔG was greatly positive as in following equation.

$$Al_2O_3 + H_2O = AlOOH \qquad \Delta G = 8.0985 \times 10^5 \ (>>0)$$

Therefore, we hypothesized that amorphous alumina films were dissolved in the subcritical water leaving different kinds of dissolved ions and reprecipitation of aluminum hydroxides took place during the cooling process. Furthermore, behavior of crystalline alumina coatings in subcritical condition and parameter dependency were needed to be investigated as further studies.

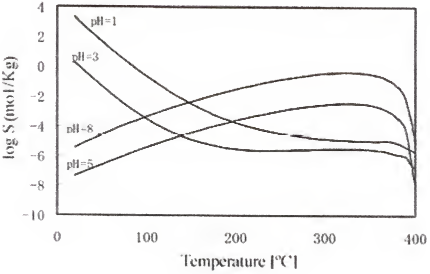

Figure 7.7. Variation of AlOOH solubility with temperature [126]

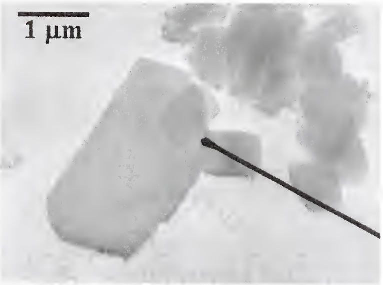

Figure 7.8. TEM image of hydrothermally grown crystallite of AlOOH in subcritical condition after autoclave test

7.3 Summary

The behavior of the sputter-deposited amorphous alumina thin films under subcritical water was reported. Uniform and smooth amorphous alumina coatings were deposited on Zircaloy substrates by RF magnetron sputter for pressurized water reactor (PWR) cladding protection. After the autoclave exposure under near-critical conditions of 20.1 MPa and 343°C, the well-faceted crystallites were grown hydrothermally with various shapes. XRD spectra showed that the major peaks corresponded to γ-AlOOH (Boehmite). The peak shifts that were observed in XPS analysis suggested the occurrence of phase transformation from oxide to hydroxide of aluminum. The shape of the boehmite was confirmed by TEM image. We hypothesized the mechanism of the boehmite formation that the amorphous alumina was dissolved in the near-supercritical water and reprecipitated during the cooling process, which wasin good agreement with the previous reports.

CHAPTER 8
CONCLUSIONS

Amorphous aluminum oxide coatings with aluminum-based compositional gradient layers (CGLs) were fabricated to develop ceramic coating corrosion protection systems for Zircaloy fuel rod cladding in pressurized water reactor (PWR) nuclear reactors. Aluminum films were deposited on Zircaloy substrates by the electron-beam evaporation and heat-treated by the controlled annealing at near the melting temperature of the aluminum. Two different annealing procedures were employed to make compositional gradient compound layers. The aluminum film thickness, air annealing time and temperature were varied. The film with the thickness of 300nm with isothermal annealing at 500°C for 2 hours in air showed that the gradient compositions of Al, Zr, and O vary through the coatings thickness by AES depth profiles. Additional annealing at 650°C for 30 min prior to isothermal annealing, described above, allowed the formation of the aluminum oxide region acting as a oxidation resistant layer as well as the intermetallic regions acting as another oxidation barrier and an interlayer for adhesion improvement. The compositional gradient layer eliminated the crack or delamination on the coating surface that were observed on the coating without CGL. Glancing angle x-ray diffraction (GAXRD) analysis showed that a variety of intermetallic and oxide phases (such as Al_3Zr, Al_2Zr_3, Al_2O_3, ZrO_2 and Zr_3O) were formed in the coatings during processing. AES multiplex spectra also showed the peak shifts in Al and O verifying the existence of multi-phases. HRTEM images and in-situ EDS data clearly showed the formation of the compositional gradient intermetallic layer structure with quite accurate stochiometry. The compositional gradient layers with Al_3Zr and Al_2Zr_3 have played a role as the adhesion improver as well as oxidation protector.

Although the stability of bulk alumina, and amorphous ceramic coatings in hydrothermal condition were reported and we completed the successful construction of compositional gradient layer structure for the improvement of adhesion, and thermal stability and for the integrated interfaces, the system in our study was not stable in near-supercritical water conditions.

The behavior of sputter-deposited amorphous alumina thin films in subcritical water was investigated. Uniform and smooth amorphous alumina coatings were deposited on Zircaloy substrates by RF magnetron sputter for PWR cladding protection. After autoclave exposure in near-supercritical condition of 20.1 MPa at 343°C, well-faceted crystallites were grown hydrothermally with various shapes. We believe that this was the first report about the behavior of amorphous alumina thin films under subcritical water conditions. XRD spectra showed the major peaks of γ-AlOOH (Boehmite). Peak shift were observed in XPS analysis indicating the change of phase from oxide to hydroxide of aluminum. We hypothesized the mechanism as the dissolution of amorphous alumina and the reprecipitation of boehmite during cooling process, which is in agreement with previous published reports.

LIST OF REFERENCES

1. W.J. Weber, R.C. Ewing, C.R.A. Catlow, T.D. de la Rubia, L.W. Hobbs, C. Kinoshita, H. Matzke, A.T. Motta, M. Mastasi, E. Salije, E.R. Vance, and S.J. Zinkle, *Journal of Materials Research*, 1998. **13**: p. 1434.

2. R.B. Wright, J. Tulenko, G. Schoessow, R. Connell, M. Dubecky, and T. Adams, *Nuclear Technology*, 1996. **115**: p. 281.

3. R.A. Graham, J.P. Tosdale, and P.T. Finden, Influence of chemical composition and manufacturing variables on autoclave corrosion of the zircaloys, *Zirconium in the Nuclear Industry. Eighth International Symposium,* ASTM STP 1023, American Society for Testing and Materials, 1989: p. 333-345.

4. W. Kim, K.S. Jung, B.H. Choi, H.S. Kwon, S.J. Lee, J.G. Han, M.I. Guseva, and M.V. Atamanov, Corrosion behavior of nitrogen-implanted zircaloy. *Surface & Coatings Technology,* 1995. **77**(1-3): p. 595-599.

5. F. He, X.D. Bai, J. Xu, S.G. Wang, J. An, Z.Y. Sun, and Y.D. Fan, The influence of yttrium ion implantation on the oxidation behavior of Zircaloy-4 at 600 degrees C. *Journal of Materials Science Letters*, 1999. **18**(9): p. 715-717.

6. X.W. Chen, X.D. Bai, H.R. Yu, Q.G. Zhou, and B.S. Chen, Effect of cerium ion implantation on the oxidation behavior of zircaloy-4 at 500 degrees C. *Nuclear Instruments & Methods in Physics Research Section B- Beam Interactions with Materials and Atoms*, 2002. **196**(3-4): p. 293-298.

7. J. Allen Haynes, E. Douglas Rigney, M.K. Ferber, and W.D. Porter, Oxidation and degradation of a plasma-sprayed thermal barrier coating system. *Surface and Coatings Technology*, 1996. **86-87**(1): p. 102-108.

8. C. Bartuli, L. Bertamini, S. Matera, and S. Sturlese, Investigation of the formation of an amorphous film at the ZrO_2-Y_2O_3/NiCoCrAlY interface of thermal barrier coatings produced by plasma spraying. *Materials Science and Engineering A*, 1995. **199**(2): p. 229-237.

9. Y. He, K.N. Lee, S. Tewari, and R.A. Miller, Development of refractory silicate-yttria-stabilized zirconia dual-layer thermal barrier coatings. *Journal of Thermal Spray Technology*, 2000. **9**(1): p. 59-67.

10. U. Leushake, T. Krell, U. Schulz, M. Peters, W.A. Kaysser, and B.H. Rabin, Microstructure and phase stability of EB-PVD alumina and alumina/zirconia for thermal barrier coating applications. *Surface and Coatings Technology*, 1997. **94-95**(1-3): p. 131-136.

11. C. Leyens, U. Schulz, B.A. Pint, and I.G. Wright, Influence of electron beam physical vapor deposited thermal barrier coating microstructure on thermal barrier coating system performance under cyclic oxidation conditions. *Surface and Coatings Technology*, 1999. **120-121**: p. 68-76.

12. J. Musil, M. Alaya, and R. Oberacker, Plasma-sprayed duplex and graded partially stabilized zirconia thermal barrier coatings: Deposition process and properties. *Journal of Thermal Spray Technology*, 1997. **6**(4): p. 449-455.

13. D.I. Pantelis, P. Psyllaki, and N. Alexopoulos, Tribological behaviour of plasma-sprayed Al_2O_3 coatings under severe wear conditions. *Wear*, 2000. **237**(2): p. 197-204.

14. G. Sundararajan, K.U.M. Prasad, D.S. Rao, and S.V. Joshi, A comparative study of tribological behavior of plasma and d-gun sprayed coatings under different wear modes. *Journal of Materials Engineering and Performance*, 1998. **7**(3): p. 343-351.

15. O. Zywitzki and G. Hoetzsch, Effect of plasma activation on the phase transformations of aluminum oxide. *Surface and Coatings Technology*, 1995. **76-77**(2): p. 754-762.

16. J.A. Thorton and J. Chin, Structure and heat treatment characteristics of sputter-deposited alumina. *Ceramic Bulletin*, 1977. **56**(5): p. 504-512.

17. B. Arsenault, B. Champagne, P. Lambert, and S. Dallaire, Zinc-nickel coatings for improved adherence and corrosion resistance. *Surface and Coatings Technology*, 1989. **37**(4): p. 369-378.

18. R. Emmerich, B. Enders, H. Martin, F. Stippich, G.K. Wolf, P.E. Andersen, J. Kudelha, P. Lukac, H. Hasuyama, and Y. Shima, Corrosion protection ability of Al2O3 coatings deposited with ion beam assisted deposition. *Surface and Coatings Technology*, 1997. **89**(1-2): p. 47-51.

19. G. Pajonk and H.D. Steffens, Corrosion behaviour of coated materials. *Fresenius Journal of Analytical Chemistry*, 1997. **358**(1-2): p. 285-290.

20. V.A.C. Haanappel, T. Fransen, B. Geerdink, P.J. Gellings, and M.F. Stroosnijder, The Properties of protective oxide scales containing cerium on alloy 800h in oxidizing and oxidizing sulfidizing environments. *Oxidation of Metals*, 1991. **35**(5-6): p. 405-414.

21. M.F. Stroosnijder, R. Mevrel, and M.J. Bennett, The interaction of surface engineering and high-temperature corrosion protection. *Materials at High Temperatures*, 1994. **12**(1): p. 53-66.

22. U. Wiklund, P. Hedenqvist, S. Hogmark, B. Stridh, and M. Arbell, Multilayer coatings as corrosion protection of Zircaloy. *Surface & Coatings Technology*, 1996. **86-7**(1-3): p. 530-534.

23. J.H. Sung, T.H. Kim, and S.S. Kim, Fretting damage of TiN coated zircaloy-4 tube. *Wear*, 2001. **250**: p. 658-664.

24. J.F. Pierson, T. Belmonte, and H. Michel, Effect of $ZrCl_4$ addition on ZrB_2 film synthesis in flowing Ar- BCl3 post-discharges. *Surface & Coatings Technology*, 2000. **133**: p. 301-306.

25. T.H. Kim, J.H. Sung, and S.S. Kim, Fretting damage behavior and mechanism of tin coated zircaloy-4 tube. *Science in China Series a-Mathematics Physics Astronomy*, 2001. **44**: p. 314-320.

26. A.K. Dua, V.C. George, and R.P. Agarwala, Thermal-conductivity of oxide coating on zircaloy-2. *Thin Solid Films,* 1980. **69**(1): p. L1-L3.

27. H.C. Chen, J. Heberlein, and E. Pfender, TEM characterization of plasma-sprayed thermal barrier coatings and ceramic-metal interfaces after hot isostatic pressing. *Thin Solid Films*, 1997. **301**(1-2): p. 105-114.

28. D.A. Shashkov, M.F. Chisholm, and D.N. Seidman, Atomic-scale structure and chemistry of ceramic/metal interfaces--I. Atomic structure of {222} MgO/Cu (Ag) interfaces. *Acta Materialia*, 1999. **47**(15-16): p. 3939-3951.

29. E. Faran, I. Gotman, and E.Y. Gutmanas, Experimental study of the reaction zone at boron nitride ceramic-Ti metal interface. *Materials Science and Engineering A*, 2000. **288**(1): p. 66-74.

30. G. Bao and H. Cai, Delamination cracking in functionally graded coating/metal substrate systems. *Acta Materialia*, 1997. **45**(3): p. 1055-1066.

31. A.S. Demirkiran and E. Avci, Evaluation of functionally gradient coatings produced by plasma-spray technique. *Surface & Coatings Technology*, 1999. **119**: p. 292-295.

32. R. Cremer and K.R. M. Witthaut, M. Schierling and D. Neuschutz, Thermal stability of Al-O-N PVD diffusion barriers. *Surface and Coatings Technology*, 2000. **108-109**(1-3): p. 48-58.

33. J.M. Schneider, W.D. Sproul, A.A. Voevodin, and A. Matthews, Crystalline alumina deposited at low temperatures by ionized magnetron sputtering. *Journal of Vacuum Science & Technology a-Vacuum Surfaces and Films*, 1997. **15**(3): p. 1084-1088.

34. S. Zhu, F. Wang, H. Lou, and W. Wu, Reactive sputter deposition of alumina films on superalloys and their high-temperature corrosion resistance. *Surface and Coatings Technology*, 1995. **71**(1): p. 9-15.

35. B.A. Beck, A Comparison of ceramic coatings proposed for corrosion protection of zircaloy cladding. *Thesis in Department of Nuclear and Radiological engineering in University of Florida,* Gainesville, 2000.

36. J.T.A. Roberts, *Structural Materials in Nuclear Power Systems*. Plenum Press, 1981.

37. E.U. Franck, Water and aqueous solutions at high pressures and temperatures. *Pure Appl. Chem.,* 1970. **24**: p. 13-30.

38. E.U. Franck, *Physicochemical properties of supercritical solvents,* Ber. Bunsenges. Phys. Chem., 1984. **88**: p. 820-825.

39. E.U. Franck, Fluids at high pressures and temperatures. *J. Chem. Thermodyn.*, 1987. **19**: p. 225-242.

40. P. Kritzer, N. Boukis, and E. Dinjus, Factors controlling corrosion in high-temperature aqueous solutions: a contribution to the dissociation and solubility data influencing corrosion processes. *Journal of Supercritical Fluids*, 1999. **15**(3): p. 205-227.

41. P. Kritzer, N. Boukis, and E. Dinjus, Corrosion of alloy 625 in high-temperature, high-pressure sulfate solutions. *Corrosion*, 1998. **54**(9): p. 689-699.

42. P. Kritzer, N. Boukis, and E. Dinjus, Corrosion of alloy 625 in aqueous solutions containing chloride and oxygen. *Corrosion*, 1998. **54**(10): p. 824-834.

43. J.W. Kysar and C.L. Briant, Crack tip deformation fields in ductile single crystals. *Acta Materialia*, 2002. **50**(9): p. 2367-2380.

44. N.C. L. Li, A. Kanthasamy, C.F. Matthews, S.W. Rollans and E.F. Gloyna, Supercritical water oxidation model development for selected EPA priority pollutants: hazardous waste management and control. *Proceedings of the 87th Annual Meeting of the Air & Waste Management Association*, Cincinnati, OH, 1994.

45. P.G.M. E. McCafferty, J.D. Ayers, and G.K. Hubler, Corrosion of metals processed by directed energy beams, C.R. Clayton and C.M. Preece, Ed.: p. 1-21. *The Metallurgical Society*, 1982.

46. P. Sioshansi, *Thin Solid Films,* 1984. **118**: p. 61-71.

47. J.H.F. G. Dearnaley, R.S. Nelson, and J. Stephen, *Ion Implantation.* North Holland, 1973.

48. C.R.C. E. McCafferty, and J. Oudar, *Fundamental aspects of corrosion protection by surface modification.* The Electrochemical Society, 1984.

49. C.M.P.a.J.K. Hirvonen, *Ion Implantation Metallurgy.* The Metallurgical Society, 1980.

50. W.A.G. V. Ashworth, and R.P.M. Proctor, *Ion Implantation Into Metals.* Pergamon Press, 1982.

51. O.W.H. G.K. Hubler, C.R. Clayton, and C.W. white, *Ion implantation and ion beam processing of materials: B.* Proceedings of the Materials Research Society, North-Holland, 1984. **27**.

52. F.A. Smidt, *Ion Implantation for Materials Processing.* Noyes Data Corporation, 1983.

53. E.M. Breinan, B.H. Kear, and C.M. Banas, *Physics Today*, 1976. **29**: p. 11,44.

54. H.E. Cline and T.R. Anthony, *Journal of Applied Physics*, 1977. **48**: p. 3895.

55. T.R. Anthony and H.E. Cline, *Journal of Applied Physics*, 1978. **49**: p. 1248.

56. P.L. Bonora, M. Bassoli, P.L.D. Anna, B. Battaglin, G.D. Mea, P. Mazzoldi, and A. Miotello, *Electrochim. Acta*, 1980. **25**: p. 1497.

57. P.G. Moore and E. McCafferty, *Journal of Electrochemical Society*, 1981. **128**: p. 1391.

58. C.W. Draper, R.E. Woods, and L.S. Meyer, *Corrosion*, 1980. **36**: p. 405.

59. R.J. Pangborn and D.R. Beaman, *Journal of Applied Physics*, 1980. **5**: p. 5992.

60. M.M. Gauthier, *Engineered Materials Handbook.* ASM International, 1994.

61. K. Oda and T. Yoshio, Hydrothermal corrosion of alumina ceramics. *Journal of the American Ceramic Society*, 1997. **80**(12): p. 3233-3236.

62. R.G. Frieser, Phase changes in thin reactively sputtered alumina films. *Journal of the Electrochemical Society*, 1966. **113**(4): p. 357-360.

63. A.L. Dragoo and J.J. Diamond, Transitions in vapor-deposited alumina from 300 to 1200 degree C. *Journal of The American Ceramic Society*, 1967. **50**(11): p. 568-574.

64. M. Kamoshida, I.V. Mitchell, and J.W. Mayer, *Applied Physics Letters*, 1971. **18**: p. 292.

65. K. Iida and T. Tsujide, *Japanese Journal of Applied Physics*, 1972. **11**: p. 840.

66. M. Koizumi, Ceram. Eng. Sci. Proc., 1992. **13**: p. 333.

67. I.B. Kaysser WA, Functionally gradient materials. *MRS Bulletin*, 1995. **20**(1): p. 22-6.

68. M. Koizumi and M. Niino, Overview of FGM research in Japan. *MRS Bulletin*, 1995. **20**(1): p. 19-21.

69. A.N.a.S. Maeda, *Recent development status of functionally gradient materials.* lSIJ Int., 1990. **30**: p. 669-703.

70. K.A. Khor, Y.W. Gu, Z.L. Dong, and T.S.S.e. al., Plasma spraying of functionally graded NiCoCrAlY/Yttria stabilized ZrO_2 coating using composite powders. *Composites and Functionally Graded Materials.* ASME International Mechanical Engineering Congress and Exposition, 1997. **80**: p. 89-105.

71. P. Kwon, M. Crimp, and M.J. Chung, Automating the design process and powder processing of functionally gradient materials. *Composites and functionally graded materials* MD, 1997. **80**: p. 73-88.

72. F. Nogata, Learning about design concepts from natural functionally graded materials. *Composites and Functionally Graded Materials*, 1997. **80**: p. 11-18.

73. A.E. Giannakopoulos, S. Suresh, and M. Finot, Elastoplastic analysis of thermal cycling - layered materials with compositional gradients. *Acta Metallurgica Et Materialia*, 1995. **43**(4): p. 1335-1354.

74. J.T. Drake, R.L. Williamson, and B.H. Rabin, Finite-element analysis of thermal residual-stresses at graded ceramic-metal interfaces .2. interface optimization for residual-stress reduction. *Journal of Applied Physics*, 1993. **74**(2): p. 1321-1326.

75. A. Kawasaki and R. Watanabe, Finite-element analysis of thermal-stress of the metal ceramic multilayer composites with controlled compositional gradients. *Journal of the Japan Institute of Metals*, 1987. **51**(6): p. 525-529.

76. S. Suresh and A. Mortensen, *Fundamentals of Functionally Graded Materials.* IOM Communications Ltd., London, 1998.

77. T. Hirai, R.J. Brook, Processing of Ceramics, Part 2: Materials science and technology. *VCH Verlagsgesellschaft*, 1996(17B): p. 297-337.

78. W.A.K. Y. Miamoto, B.H. Rabin, A. Kawasaki, R.G. Ford, *Functionally Graded Materials: Design, Processing and Applications.* Kluwer Academic Publishers, Boston, London, 1999: p. 248-252.

79. A. Mortensen and S. Suresh., Functionally graded metals and metal-ceramic composites: part 1 processing. *International Materials Reviews,* 1995. **40**(6): p. 239-265.

80. P. Sajgalik and Z. Lences, *Key Engineering Materials.* Trans. Tech. Publ. Ltd., Switzerland, 2000. **175,176.**

81. S.H. R. Slowak, R. Liedtke and R. Waser, *Integrated Ferroelectrics*, 1999. **24**(1-4): p. 169-179.

82. W.A. Kaysser, Proceedings of the Fifth International Symposium on Functionally Graded Materials, Dresden, Germany, 26-29 October 1998, *Materials Science Forum* 308-311, 1999(Trans. Tech. Publications Ltd., Switzerland).

83. Willert-Porada, *Materials Science Forum*, 1999. **308-311**: p. 806-813.

84. U. Birth, *Materials Science Forum*, 1999. **308-311**: p. 766-773.

85. R. Jedamzik, *Materials Science Forum*, 1999. **308-311**: p. 782-786.

86. Y.M. Shiota, *Proceedings of the Fourth International Symposium on Functionally Graded Materials*, Tsukuba, Japan, 21-24 October, 1996, Elsevier, Amsterdam, 1997.

87. K. K. Trumble, I. Reimanis and S. Sampath, *Proceedings of the Sixth International Symposium on Functionally Graded Materials*, Estes Park, CO, USA, 10-14 September 2000, 2001. **114**(Ceram. Trans.): p. 114.

88. W.A. Kaysser, M. Peters, U. Schulz, C. Drasar, *Proceedings of the CIMTEC 2002, Part B*, Florence, Italy, 14-18 July 2002, Academy of Ceramics, International Ceramic Federation, Faenza, 2002: p. 341-353.

89. D. Nunz and Y.Y. Yang, Stress singularities at the interface in bonded dissimilar materials under mechanical and thermal loading. *J. Appl. Mech.*, 1992. **59**: p. 857?861.

90. Y.D. Lee and F. Erdogan, Residual/thermal stress in FGM and laminated thermal barrier coatings. *Int. J. Fract.,* 1995. **69**: p. 145-165.

91. L.C. Feldman, *Fundamentals of surface and thin film analysis.* North-Holland, 1986.

92. C.R. Brundle and C.A. Evans, *Encyclopedia of Materials Characterization : surfaces, interfaces, thin films.* Butterworth-Heinemann, 1992.

93. P.A. Steinmann, *Thin Solid Films*, 1987. **154**: p. 333.

94. C.C. Shih, S.J. Lin, K.H. Chung, Y.L. Chen, and Y.Y. Su, Increased corrosion resistance of stent materials by converting current surface film of polycrystalline oxide into amorphous oxide. *Journal of Biomedical Materials Research*, 2000. **52**(2): p. 323-332.

95. P.T. Stroud, Ion-bombardment and implantation and their application to thin-films. *Thin Solid films*, 1972. **11**(1): p. 1.

96. A.W. Mullendore, J.B. Whitley, and D.M. Mattox, Thermal Fatigue Testing Of Coatings For Fusion-Reactor Applications. *Thin Solid Films*, 1981. **83**(1): p. 79-85.

97. J.W. Patten, Mcclanah, E D, Johnston, J W, Room-Temperature Recrystallization In Thick Bias-Sputtered Copper Deposits. *Journal of Applied Physics*, 1971. **42**(11): p. 4371.

98. R.D. Thompson, Takai H, Psaras P A, Tu K N, Effect of a substrate on the phase-transformations of amorphous TiSi2 thin-films. *Journal of Applied Physics*, 1987. **61**(2): p. 540-544.

99. V.I. Dybskov, Reaction diffusion in heterogeneous binary-systems .1. Growth of the chemical-compound layers at the interface between 2 elementary substances - one compound layer. *Journal of materials science*, 1986. **21**(9): p. 3078-3084.

100. R.N. Singh, Interdiffusion and compound , formation in the Mo/Pd/Si thin-film metallization system. *Thin solid films*, 1986. **143**(3): p. 249-257.

101. K. Ehrlich, J. Konys, and L. Heikinheimo, Materials for high performance light water reactors. *Journal of Nuclear Materials*, 2004. **327**(2-3): p. 140-147.

102. R. Baney, R. Singh, G. Fuchs, and J. Tulenko, *An Innovative Ceramic Based Corrosion Protection System for Zircaloy Cladding.* Project Proposal, 1999: p. University of Florida, Gainesville, FL.

103. R.F. Bunshah, *Handbook of Deposition Technologies for Films and Coatings.* Noyes publication, **2nd ed.,**1994.

104. B.A. Movchan and A.V. Demchishin, Study of the structure and properties of thick vacuum consensates of nickel, titanium, tungsten, aluminum oxide and zirconium dioxide. *Phys. Met. Metallogr.,* 1969. **28**(4): p. 83-90.

105. W.J. Tomlinson and M.W. Carroll, Substrate roughness, deposit thickness and the corrosion of electroless nickel coatings. *Journal of Materials Science*, 1990. **25**(12): p. 4972-4976.

106. S.E. Hernandez, A.J. Griffin, F.R. Brotzen, and C.F. Dunn, The effect of thickness on the corrosion susceptibility of al thin-film metallizations. *Journal of the Electrochemical Society*, 1995. **142**(4): p. 1215-1220.

107. M. Nordin, M. Herranen, and S. Hogmark, Influence of lamellae thickness on the corrosion behaviour of multilayered PVD TiN CrN coatings. *Thin Solid Films*, 1999. **348**(1-2): p. 202-209.

108. K. Loucif, P. Merle, and R. Borrelly, On the thermoelectric-power variation according to temperature of zirconium alloys and its possible application to the estimation of the amount of solubility variations of iron and chromium in zircaloy. *Journal of Nuclear Materials*, 1993. **202**(1-2): p. 193-196.

109. L. Xiao and H.C. Gu, Dislocation structures in zirconium and zircaloy-4 fatigued at different temperatures. *Metallurgical and Materials Transactions a-Physical Metallurgy and Materials Science*, 1997. **28**(4): p. 1021-1033.

110. B. Ollivier and A. Matthews, *Adhesion Measurements of Films and Coatings,* 1995: p. 103-114.

111. X. Nie, A. Leyland, H.W. Song, A.L. Yerokhin, S.J. Dowey, and A. Matthews, Thickness effects on the mechanical properties of micro-arc discharge oxide coatings on aluminium alloys. *Surface and Coatings Technology*, 1999. **116-119**: p. 1055-1060.

112. A. Perry, Adhesion studies of ion-plated on steel. *Thin Solid Films*, 1981. **81**: p. 357-366.

113. D. Butler, C. Stoddart, and P. Stuart, The stylus or scratch method for thin film adhesion measurement: some observation and comments. *Journal of Applied Physics,* 1970. **D3**(877-883).

114. M.W.J. Chase, *NIST-JANAF thermochemical tables.* 1998. **4th ed.**

115. A. Laik, K. Bhnumurthy, and G.B. Kale, Intermetallics in the Zr-Al diffusion zone. *Intermetallics*, 2003. **12**: p. 69-74.

116. W. Deqing, J. Neumann, and H. Lopez, Reactive synthesis of in-situ $ZrAl_3$-Al_2O_3-Al composites. *Metallurgical and Materials Transactions A-Physical Metallurgy and Materials Science*, 2003. **34A**(6): p. 1357-1360.

117. H. Yanagisawa and A. Noya, Diffusion barrier effects of Al_3Zr/Zr bilayered films interposed between Al and Si. *Electronics and Communications in Japan*, Part 2, 1996. **79**(9): p. 170-175.

118. P.E. Savage, S. Gopalan, T.I. Mizan, C.J. Martino, and E.E. Brock, Reactions at supercritical conditions - applications and fundamentals. *Aiche Journal,* 1995. **41**(7): p. 1723-1778.

119. R.L. Smith, P. Atmaji, Y. Hakuta, M. Kawaguchi, T. Adschiri, and K. Arai, Recovery of metals from simulated high-level liquid waste with hydrothermal crystallization. *Journal of Supercritical Fluids*, 1997. **11**(1-2): p. 103-114.

120. S.B. Hawthorne, Y. Yang, and D.J. Miller, Extraction of Organic Pollutants from Environmental Solids with Subcritical and Supercritical Water. *Analytical Chemistry*, 1994. **66**(18): p. 2912-2920.

121. D.W. Matson and R.D. Smith, Supercritical fluid technologies for ceramic-processing applications. *Journal of the American Ceramic Society*, 1989. **72**(6): p. 871-881.

122. H.J. Bleyl, J. Abeln, N. Boukis, H. Goldacker, M. Kluth, A. Kruse, G. Petrich, H. Schmieder, and G. Wiegand, Hazardous waste disposal by supercritical fluids. *Separation Science and Technology*, 1997. **32**(1-4): p. 459-485.

123. K.A. Dinov and K. Kasahara, Thermodynamic study in support of pressurized water reactor specific reactor water chemistry. *Nuclear Technology*, 1996. **115**(1): p. 81-90.

124. R. Bauch, M. Cambini, P. Weisgerber, C. Deasmundis, and C. Plog, Investigations on oxide formed in high-temperature water on austenitic steel. *Journal of Nuclear Materials,* 1980. **92**(2-3): p. 334-344.

125. T. Adschiri, K. Kanazawa, and K. Arai, Rapid and continuous hydrothermal synthesis of boehmite particles in subcritical and supercritical water. Journal of the American Ceramic Society, 1992. **75**(9): p. 2615-2618.

126. T. Adschiri, Y. Hakuta, K. Sue, and K. Arai, Hydrothermal synthesis of metal oxide nanoparticles at supercritical conditions. *Journal of Nanoparticle Research*, 2001. **3**(2-3): p. 227-235.

BIOGRAPHICAL SKETCH

Sang Tae Park was born in Seoul, South Korea, in 1971. He graduated from the Unnam High School in 1989 and entered Korea University to study materials science and engineering. In 1992, he had been in Korea Army serving as a corps guard. After that he came back to campus and received his bachelor' degree in 1996. He joined the master program in the same university and completed his research on non-volatile ferroelectric memory device using ferroelectric materials and eared his master degree in 1998. After graduation, he did research in the Center for Semiconductor Technology in Korea University until he joined the Ph.D program in the Department of Materials Science and Engineering in University of Florida.

I certify that I have read this study and that in my opinion it conforms to acceptable standards of scholarly presentation and is fully adequate, in scope and quality, as a dissertation for the degree of Doctor of Philosophy.

Ronald H. Baney

Ronald H. Baney, Chair
Research Scientist of Materials Science and
Engineering

I certify that I have read this study and that in my opinion it conforms to acceptable standards of scholarly presentation and is fully adequate, in scope and quality, as a dissertation for the degree of Doctor of Philosophy.

E. Dow Whitney

E. Dow Whitney
Emeritus Professor of Materials Science and
Engineering

I certify that I have read this study and that in my opinion it conforms to acceptable standards of scholarly presentation and is fully adequate, in scope and quality, as a dissertation for the degree of Doctor of Philosophy.

Paul Holloway

Paul H. Holloway
Distinguished Professor of Materials
Science and Engineering

I certify that I have read this study and that in my opinion it conforms to acceptable standards of scholarly presentation and is fully adequate, in scope and quality, as a dissertation for the degree of Doctor of Philosophy.

Darryl R. Butt
Associate Professor of Materials Science
and Engineering

I certify that I have read this study and that in my opinion it conforms to acceptable standards of scholarly presentation and is fully adequate, in scope and quality, as a dissertation for the degree of Doctor of Philosophy.

James S. Tulenko

James S. Tulenko
Professor of Nuclear and Radiological
Engineering

This dissertation was submitted to the Graduate Faculty of the College of Engineering and to the Graduate School and was accepted as partial fulfillment of the requirements for the degree of Doctor of Philosophy.

August 2004

Pramod Khargonekar

Pramod P. Khargonekar
Dean, College of Engineering

Kenneth J. Gerhardt
Interim Dean, Graduate School